ALDRICH®
Materials Science

Magnetic Materials
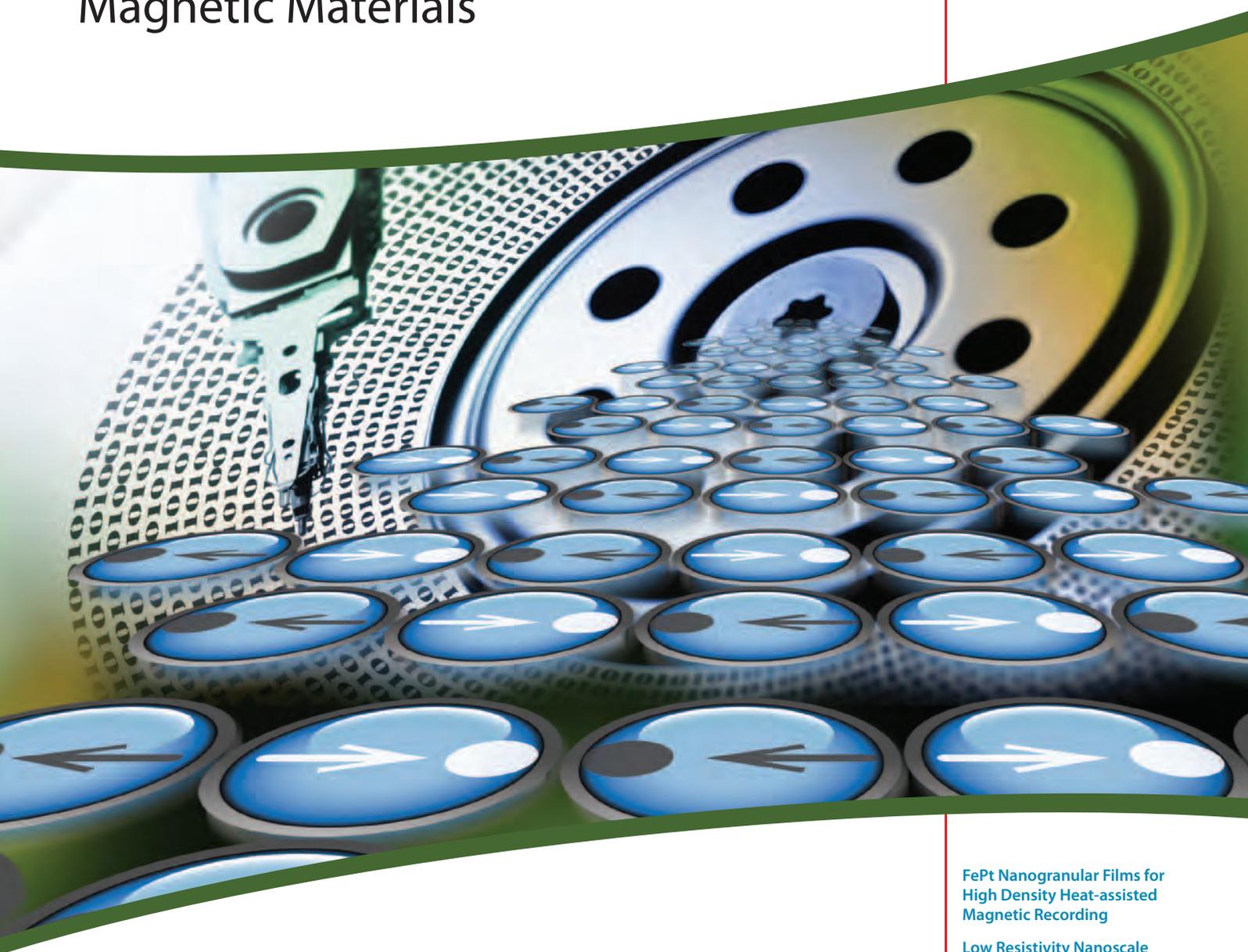
A New Spin on Magnetic Materials

SIGMA-ALDRICH®

Introduction

Welcome to the second issue of *Material Matters*™ for 2013 focusing on synthesis, characterization, and applications of magnetic materials. Far from a mere curiosity, magnetic compounds play a vital role in modern technology such as information storage. The ability to store information in spin rather than charge enables a more rapid response and requires less energy input. In recent years, the potential of materials which combine multiple magnetic properties have been demonstrated to reduce energy consumption and enhance technologies performance, including refrigeration and actuators.

Adam Raw, Ph.D.
Aldrich Materials Science

In our first article, Professor Kazuhiro Hono (National Institute for Materials Research, Japan) discusses one of the most important current applications for magnetic materials, magnetic recording. Modern advances in computation have been driven by the continuous increase of recording density. However, current technology is rapidly approaching the theoretical density limit. This article discusses new technologies with the potential to continue to increase recording density through heat-assisted magnetic recording and the implementation of new recording materials.

Professor Bethanie Stadler (University of Minnesota, USA), in our second article, describes a synthetic route to one-dimensional inorganic nanostructures and their potential applications. Through template-directed synthesis, conductive and magnetostrictive nanowires with well-defined morphology and exceedingly smooth surfaces can be formed. These nanowires demonstrate superior conductivity to those freely assembled in solution as well as allowing for synthesis of higher-density materials.

In the third article, Professor S.B. Roy (Raja Ramanna Centre for Advanced Technology, India) reviews multifunctional magnetic materials and their technological applications. Multifunctional materials combine magnetic properties such as giant magneto-resistance, magnetostriction, and the magnetocaloric effect in a single compound. Presented here are measurements of the Heusler alloy $Ni_{50}Mn_{34}In_{16}$, which demonstrates all three of the aforementioned properties.

Our fourth article, contributed by Professor Thomas Lograsso (Ames Laboratory, USA), discusses techniques and challenges of crystal growth of magnetic alloys. Uniform defect-free samples of these materials are necessary to fully characterize their magnetic properties. The growth of large single crystals through proper selection of growth conditions and techniques allows for understanding fundamental properties of these technologically important materials and the role of orientation on potential device performance.

Finally, Professor K.G. Suresh (IIT Technology Bombay, India) presents an overview of the state of current magnetic research. A greater understanding of the origin and control of magnetic properties, combined with constant improvement in magnetic memory, has led to the discovery of many novel magnetic compounds and applications. Spintronics, exchange bias, and the magnetocaloric effect are finding applications in next generation random access memory, transducers, and solid-state refrigerators. These magnetic properties are poised to alter the design of modern technology.

Each article in this publication is accompanied by a list of relevant materials available from Aldrich® Materials Science. For additional product information, please visit Aldrich Materials Science at **aldrich.com/matsci**. Please send us your comments or suggestions for *Material Matters*™ or your product suggestions at *matsci@sial.com*.

About Our Cover

Magnetic materials are essential components in devices and have driven advances in magnetic storage, refrigeration, sensing and motors. The cover art of this issue depicts the progression from the ordering of individual spins to the storage of information in a hard disc drive. This translation of information from magnetic to electronic data is a central component of modern information infrastructure and poised for continued expansion through the use of spintronic devices and materials.

Table of Contents

Articles

Featured Products

Your Materials Matter

Bryce P. Nelson, Ph.D.
Aldrich Materials Science Initiative Lead

*We welcome fresh product ideas from you. Do you have a material or compound you wish to see in our Aldrich® Materials Science line? If it is needed to accelerate your research, it matters. Send your suggestion to **matsci@sial.com** for consideration.*

Dr. Ralf Meyer of the Technische Universität München, Germany, recommended the addition of high purity Aluminum Ingots **(Aldrich Prod. No. 773964)** to our catalog for use in Molecular Beam Epitaxy (MBE). Aluminum is frequently used in MBE to form aluminum nitride[1] or heterostructures with materials such as GaAs[2]. In addition, aluminum nitride thin films are utilized as piezoelectrics for microelectromechanical systems.[3] Moreover, the high trace metals purity of this product (99.99995%) makes it ideal for the synthesis of III-V semiconductors, where small amounts of dopants can have a disproportionate impact on properties.[4]

References

(1) Brubaker, M.D.; Levin, I.; Davydov, A.V.; Rourke, D.M.; Sanford, N.A.; Bright, V.M.; Bertness, K.A. *Journal of Applied Physics* **2011**, *110(5)*, 053506/1-053506/7.
(2) Fan, D.; Zeng, Z.; Hu, X.; Dorogan, V.G.; Li, C.; Benamara, M.; Hawkridge, M.E.; Mazur, Y.I.; Yu, S.Q.; Johnson, S.R.; et al. *Applied Physics Letters* **2012**, *101(18)*, 181103/1-181103/4.
(3) Doppalapudi, D.; Mlcak, R.; Chan, J.; Tuller, H.; Bhattacharya, A.; Moustakas, T. *Materials Research Society Symposium Proceedings* **2004**, *798*, 403-408.
(4) Unuma, T.; Yoshita, M.; Noda, T.; Sakaki, H.; Akiyama, H. *Journal of Applied Physics* **2003**, *93(3)*, 1586-159

Aluminum

[7429-90-5]   Al   FW 26.98

resistivity	2.6548 µΩ-cm
mp	660.37 °C
density	2.7 g/mL, 25 °C
bp	2460 °C
ait	1400 °F

▶ **ingot, L 10 mm × W 7 mm, 99.99995% trace metals basis**

773964-5EA	5 ea

FePt Nanogranular Films for High Density Heat-assisted Magnetic Recording

Kazuhiro Hono
National Institute for Materials Research
Tsukuba 305-0047, Japan
Email: kazuhiro.hono@nims.go.jp

Introduction

A hard disk drive (HDD) is a data storage device that stores digital information by magnetizing nanosized magnets on flat disks and retrieves data by sensing the resulting magnetic field. HDDs have been the predominant storage device in computers for the past 50 years. Although solid-state devices (SSD) are now meeting an increasing portion of the storage needs of portable computers, HDD technology are expected to continue to play a major role in handling the ever increasing digital data necessary for cloud computing. The number of HDDs sold in 2012 was approximately 800 million, nearly one tenth of the world's population!

A HDD is comprised of one or more rigid disks with magnetic heads supported on actuator arms to write and read digital information. The disk rotates at a very fast rate (~7,000 rpm) with a small magnetoresistive head scanning the disk within a distance of a few nanometers. The unit of areal density of recording is the number of bits per square inch (bpsi) and that of a current HDD is ~700 Gbpsi. The higher the areal density, the more data stored in the same volume. In the past, the density of HDDs increased by 100% every year, but recent growth rates have slowed to 25%. Although various technological improvements have been made in both recording heads and media in the current perpendicular magnetic recording (PMR) system, ~1 Tbpsi is considered to be the limit for the PMR method. Thus, a transition to a new magnetic recording method must be made in the near future to continue the trend toward 4 Tbpsi or higher.

New Technologies

Heat assisted magnetic recording (HAMR) is a promising technology for achieving this goal. However, for this method to be successful, new media using a high magnetocrystalline anisotropy material must be developed. The current recording media are $CoCrPt-SiO_2$ nanogranular films, in which nanosized CoCrPt alloy particles with hcp structure are dispersed uniformly with a strong preferred orientation of [0001] as shown in **Figure 1**.
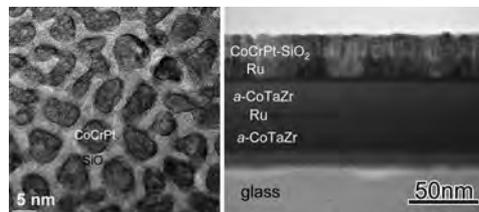
Figure 1. Transmission electron microscopy (TEM) planar image of $CoCrPt-SiO_2$ recording layer and the cross-sectional image of the currently used perpendicular recording media. CoCrPt ferromagnetic particles of ~6 nm are dispersed in SiO_2. On the glass substrate, amorphous-CoTaZr soft-magnetic underlayer, the Ru interlayer that aligns the [0001] axis in the perpendicular to the film are grown. CoCrPt grains are grown on Ru grains epitaxially with the strong [0001] texture.

Such films are deposited on glass substrates with an amorphous CoTaZr soft-magnetic underlayer (SUL) and a Ru interlayer that optimize the grain size and the crystallographic orientation of the CoCrPt grains. Since the easy axis of magnetization of the CoCrPt alloy is the [0001] direction, this crystallographic texture gives rise to strong perpendicular magnetic anisotropy. Each grain is magnetically isolated and one bit contains multiple CoCrPt grains that are magnetized in the same direction as shown in **Figure 2**.
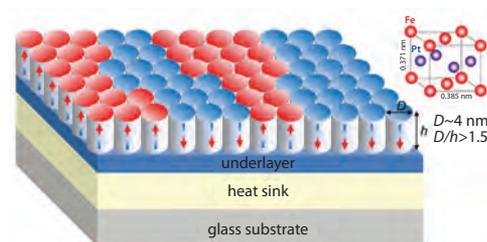
Figure 2. Ideal media structure for HAMR. Red and blue colors show the direction of magnetic poles, and their boundary is the magnetic domains that separate the neighboring bits. The $L1_0$-FePt (the upper right figure) must grow in columns separated by the nonferromagentic "segregant." The column diameter and height ratio D/h must be higher than 1.5, and a diameter of less than 4 nm is desired.

To obtain a sufficient signal-to-noise ratio for a bit density of 1 Tbpsi, more than 10 ferromagnetic particles must be contained in an area of ~25 × 25 nm. Therefore, the ferromagnetic particles must be refined further to ~4 nm to achieve an areal density above 1 Tbpsi. This requirement makes the ferromagnetic particles thermally unstable as the magnetocrystalline energy K_uV becomes comparable to the thermal energy k_BT, where K_u is the magnetocrystalline constant, V is the volume of the particle, and k_B is the Boltzman constant. In order to store recorded information for longer than 10 years, the value of K_uV/k_BT must be larger than 60. This means that a ferromagnetic material with high magnetocrystalline anisotropy must be used for high density recording as V becomes very small. While the K_u of CoCrPt alloys is ~0.3 MJ/m^3, the $L1_0$-ordered FePt has a one order of magnitude larger magnetocrystalline anisotropy of 6.6 MJ/m^3, which makes the minimum size of stable ferromagnetic particles ~4 nm for spheres and 2.4 nm for cylinders.[1] However, as the size of the hard magnetic particles is reduced, the magnetic field required to magnetize the particle increases enormously. The typical switching field for the current recording media is about 0.8 T, while the magnetic field to switch the magnetization of the nanosized hard magnet will be greater than 3 T. However, the highest magnetic field that can be generated using a write head (a small electromagnet) is limited to about 1.5 T. This means the nanosized particles of hard magnetic materials are not writable. This dilemma is known as the "trilemma" of magnetic recording: ultrahigh density magnetic recording requires nanosized ferromagnetic particles, but this requirement makes

them thermally unstable. To overcome this problem, a high K_u material must be used; however, switching the field of the particles causes them to be become too large to write. Thus, the magnetization switching requires energy assistance. Heat-assisted magnetic recording (HAMR) uses heat to achieve the magnetization switching of high K_u particles with thermal energy using a well-focused laser beam.[2] At elevated temperature, writing can be accomplished using the magnetic field that can be generated with a write head. When temperature decreases after writing, the high K_u of the nanosized particle has sufficient thermal stability for permanent recording.

New technologies are necessary in both the head and medium to realize HAMR. The HAMR head has been previously demonstrated using a plasmonic antenna.[3] However, a suitable magnetic recording medium to demonstrate the feasibility of high-density HAMR recording has not been successfully produced until recently. The desirable HAMR media should be made of densely dispersed ferromagnetic particles of high magnetocrystalline anisotropy with a uniform particle size of 4-6 nm with columnar grains of the aspect ratio $D/h > 1.5$ as shown in **Figure 2**. Among various hard magnetic materials, $L1_0$-ordered FePt has been considered to be the most promising since it has excellent corrosion resistance. In addition, the film must exhibit high coercivity above 3 T, more than four times larger than that of the current recording media.

Technological Challenges of Deposition

The most critical issue for developing a HAMR recording medium is to achieve a $L1_0$ chemical order in FePt particles of 4–5 nm with the easy axis of magnetization [001] perpendicular to the film plane. When FePt is sputter-deposited with oxides, we can disperse nanoparticles in oxides easily; however, the FePt phase is the fcc disordered A1 phase while the structure of the equilibrium phase is $L1_0$. When the films are annealed after the sputter deposition, the A1 phase transforms to the $L1_0$ phase; at the same time, particle coarsening occurs and the desired nano-granular structure with a narrow size distribution is totally destroyed. In 2008, our group established a way to fabricate perpendicular magnetic thin films with FePt particles of a 5.5 nm mean diameter and a 2.3 nm size dispersion on thermally oxidized Si substrates (Aldrich Prod. No. 646687) using the magnetron sputtering technique as shown in **Figure 3**.[4]
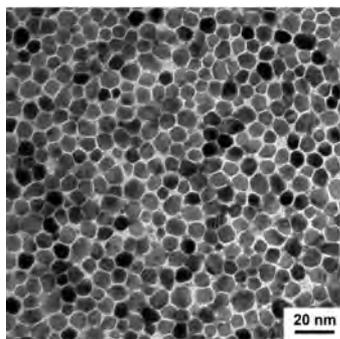
Figure 3. TEM image of the FePt-C granular thin film grown on an MgO underlayer on a thermally oxidized Si substrate. The first encouraging media structure with ~6 nm FePt particles uniformly dispersed with a narrow size distribution.[4]

The key was to sputter-deposit FePt and C on a heated substrate so the ordering to the $L1_0$ structure can progress during the film growth at a much lower temperature than that required for the post-deposition annealing of A1-FePt. At the same time, C phase separates from FePt forming a thin channel of amorphous carbon. However, the coercivity of this material was only in the order of 0.8-1.5 T due to the low degree of the $L1_0$ order in the FePt particles, and a higher coercivity had to be achieved for successful HAMR media. Recently we succeeded in processing a nanoparticle-dispersed perpendicular magnetic thin film with a mean particle diameter of 6.1 nm, size dispersion of 1.8 nm, and

coercivity of 3.7 T by adding Ag to the FePt-C granular films.[5] To align the [001] crystal orientation perpendicular to the film, a thin layer of MgO was grown on a Si substrate, followed by sputtering a FePt-C magnetic layer. This film had the highest grade of particle dispersion and crystal alignment of $L1_0$-FePt particles. Subsequent static tester results measured at the HGST San Jose Research Center have shown that 550-Gbpsi HAMR recording is possible on this medium as shown in **Figure 4**.[5] This recording density was the highest one achieved by HAMR and was comparable to that of conventional perpendicular magnetic recording method at that time.
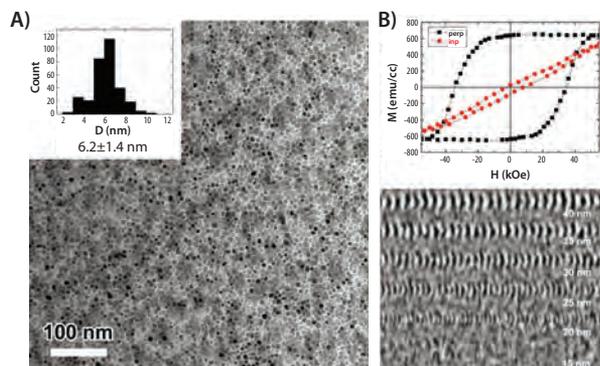
Figure 4. **A)** TEM image of the $(FePt)_{0.9}Ag_{0.1}$-40 vol% C granular film; **B)** static magnetization curves, and the patterns of recording bits by the static HAMR head. The mean particle diameter of the FePt particles is 6.1 nm, and their size dispersion is 1.8 nm. Coercivity is 3.7 T, which is more than five times higher than that of the conventional magnetic recording media. In the recording pattern with the static HAMR head, 15-nm bits were observed with a bit width of 92 nm. Converted to a recording density, this is equivalent to 550 Gbpsi.[6]

Summary

Since (FePt)Ag-C nanogranular films can be deposited easily by sputtering on the MgO interlayer, where crystal orientations are naturally aligned to the [001] direction during the film growth, the (FePt)Ag-C films can be fabricated on substrates other than Si, including glass. From this viewpoint, the technology has high potential to be extended to industrially viable production lines in the future and can be considered to be an important advancement toward the practical application of FePt-based HAMR media. However, there are still a few challenges that need to be resolved: one is to limit the surface roughness and another is to grow the FePt grains in a columnar shape with an aspect ratio D/h of at least 1.5 as shown in **Figure 2**. Thorough investigations on the FePt-C system have led to the conclusion that we need to seek a new segregant material to replace C. Another issue is the slow growth rate of the MgO insulator by RF sputtering. We recently tested an electrically conductive underlayer, MgTiO, to develop a FePt [001] that can be grown with DC sputtering, and expect to eventually achieve the ideal nanostructure as shown in **Figure 2**. Moreover, Seage has recently announced a 1-Tbpsi HAMR recording. Thus, commercial implementation of HAMR appears to be right around the corner.

References

(1)   Weller, D.; Moser, A., *IEEE Trans. Magn.*, **1999**, *35*, 4423.
(2)   Rottmayer, R.E.; Batra, S.; Buechel, D.; Challener, W.A.; Hohlfield, J.; Kubota, Y.; Lu, B.; Michalcea, C.; Mountfield, K.; Pelhos, K.; Peng, C.; Rausch, T.; Seigler, M. A.; Weller, D.; Yang, X.M., *IEEE Trans. Magn.*, **2006**, *42*, 2417.
(3)   Stipe, B.C.; Strand, T.C.; Poon, C.C.; Balamane, H.; Boone, T.D.; Katine, J.A.; Li, J.L.; Rawat, V.; Nemoto, H.; Hirotsune, A.; Hellwig, O.; Ruiz, R.; Dobisz, E.; Kercher, D.S.; Robertson, N.; Albrecht, T.R.; Terris, B.D., *Nature Photon.*, **2010**, *4*, 484.
(4)   Perumal, A.; Takahashi, Y.K.; Hono, K., *Appl. Phys. Exp.*, **2008**, *1*, 101301.
(5)   Zhang, L.; Takahashi, Y.K.; Perumal, A.; Hono, K., *J. Magn. Magn. Mater.*, **2010**, *322*, 2658.
(6)   Zhang, L.; Takahashi, Y.K.; Hono, K.; Stipe, B.C.; Juang, J.-Y.; Grobis, M., *IEEE Trans. Magn.*, **2011**, *47*, 4062.
(7)   http://www.seagate.com/about/newsroom/press-releases/terabit-milestone-storage-seagate-master-pr/

For questions, product data, or new product suggestions, contact Aldrich Materials Science at matsci@sial.com.

37

Substrates for Thin Film Deposition

For a complete list of available materials, visit aldrich.com/substrates.

Name	Composition	Dimensions	Orientation	Prod. No.
Aluminum oxide	Al_2O_3	10 × 10 × 0.5 mm	<0001>	634875-1EA 634875-5EA
Gallium antimonide	GaSb	diam. × thickness 2 in. × 0.5 mm	<100>	651478-1EA
Gallium arsenide	GaAs	diam. × thickness 2 in. × 0.5 mm	<100>	651486-1EA
Gallium phosphide	GaP	diam. × thickness 2 in. × 0.5 mm	<111>	651494-1EA
Lanthanum aluminum oxide	$LaAlO_3$	10 × 10 × 0.5 mm	<100>	634735-1EA
Magnesium aluminate	$MgO·Al_2O_3$	10 × 10 × 0.5 mm	<100>	635073-1EA
Magnesium aluminate	$MgO·Al_2O_3$	10 × 10 × 0.5 mm	<110>	634840-1EA
Magnesium aluminate	$MgO·Al_2O_3$	10 × 10 × 0.5 mm	<111>	634832-1EA
Magnesium oxide	MgO	L × W × thickness 10 × 10 × 0.5 mm	<100>	634646-1EA
Magnesium oxide	MgO	L × W × thickness 10 × 10 × 0.5 mm	<111>	634697-1EA
Silicon	Si	diam. × thickness 2 in. × 0.5 mm	<100>	646687-1EA 646687-5EA
Silicon	Si	diam. × thickness 3 in. × 0.5 mm	<100>	647535-1EA 647535-5EA
Silicon	Si	diam. × thickness 2 in. × 0.5 mm	<111>	647101-1EA 647101-5EA
Silicon dioxide	SiO_2	L × W × thickness 10 × 10 × 0.5 mm	<0001>	634867-5EA
Strontium lanthanum aluminate	$SrLaAlO_4$	10 × 10 × 0.5 mm	<001>	634891-1EA
Strontium titanate	$SrTiO_3$	10 × 10 × 0.5 mm	<110>	634670-1EA
Strontium titanate	$SrTiO_3$	10 × 10 × 0.5 mm	<111>	638161-1EA
Strontium titanate	$SrTiO_3$	10 × 10 × 0.5 mm	<100>	634689-1EA
Titanium(IV) oxide, rutile	TiO_2	L × W × thickness 10 × 10 × 0.5 mm	<001>	635057-1EA
Titanium(IV) oxide, rutile	TiO_2	L × W × thickness 10 × 10 × 0.5 mm	<100>	635049-1EA
Titanium(IV) oxide, rutile	TiO_2	L × W × thickness 10 × 10 × 0.5 mm	<110>	635065-1EA

Sputtering Targets

For a complete list of available materials, visit aldrich.com/pvd.

Name	Diam. × Thickness (in.)	Purity (%)	Prod. No.
Aluminum	3.00 × 0.125	99.9995	749036-1EA
Aluminum zinc oxide	3.00 × 0.125	99.99	752665-1EA
Chromium	3.00 × 0.125	99.95	749052-1EA
Gallium zinc oxide	3.00 × 0.125	99.99	752673-1EA
Indium oxide	3.00 × 0.125	99.99	752649-1EA
Indium tin oxide	3.00 × 0.125	99.99	752657-1EA
Indium zinc oxide	3.00 × 0.125	99.99	752703-1EA
Titanium	3.00 × 0.125	99.995	749044-1EA
Zinc	3.00 × 0.125	99.995	749060-1EA
Zinc oxide	3.00 × 0.125	99.99	752681-1EA

Vapor Deposition Precursors for Magnetic Thin Film Formation

For a complete list of available materials, visit aldrich.com/vapordeposition.

Cobalt

Name	Structure	Purity (%) and Grade	Prod. No.
Bis(cyclopentadienyl)cobalt(II)		-	339164-2G 339164-10G
Bis(ethylcyclopentadienyl)cobalt(II)		-	510645-1G
Bis(pentamethylcyclopentadienyl)cobalt(II)		-	401781-1G
trans-Dinitrobis(ethylenediamine)cobalt(III) nitrate		-	575887-5G
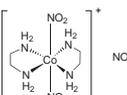
Chromium

Name	Structure	Purity (%) and Grade	Prod. No.
Bis(pentamethylcyclopentadienyl)chromium(II)		96	475165-1G

Iron

Name	Structure	Purity (%) and Grade	Prod. No.
Bis(pentamethylcyclopentadienyl)iron(II)		97	378542-1G 378542-5G
1,1′-Diethylferrocene		98	517445-5ML
Iron(0) pentacarbonyl	$Fe(CO)_5$	>99.99	481718-25ML 481718-100ML

Molybdenum

Name	Structure	Purity (%) and Grade	Prod. No.
[1,1′-Bis(diphenylphosphino)ferrocene]tetracarbonyl-molybdenum(0)		96	555118-1G 555118-5G

Platinum

Name	Structure	Purity (%) and Grade	Prod. No.
Trimethyl(methylcyclopentadienyl)platinum(IV)		98	645605-2G
Trimethyl(methylcyclopentadienyl)platinum(IV)		packaged for use in deposition systems	697540-10G

Silicon

Name	Structure	Purity (%) and Grade	Prod. No.
(3-Aminopropyl)triethoxysilane		≥98.0	741442-100ML 741442-500ML
Hexamethyldisilazane		99.9	379212-25ML 379212-100ML
Hexamethyldisilazane		≥99	440191-100ML 440191-1L
Silicon tetrachloride	$SiCl_4$	99.998	289388-100ML 289388-800ML
2,4,6,8-Tetramethylcyclotetrasiloxane		≥99.999 ≥99.5	512990-25ML 512990-100ML
Tetramethylsilane		≥99.99	523771-100ML

For questions, product data, or new product suggestions, contact Aldrich Materials Science at **matsci@sial.com**.

ALDRICH®
Materials Science

39

Name	Structure	Purity (%) and Grade	Prod. No.
Tris(*tert*-butoxy)silanol		99.999	553468-5G 553468-25G
Tris(*tert*-pentoxy)silanol		≥99.99	553441-5G 553441-25G
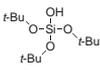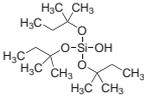
Tantalum

Name	Structure	Purity (%) and Grade	Prod. No.
Pentakis(dimethylamino)tantalum(V)		99.99	496863-5G
Tris(diethylamido)(*tert*-butylimido)tantalum(V)		99 ≥99.99 trace metals basis	521280-5ML
Tris(diethylamido)(*tert*-butylimido)tantalum(V)		packaged for use in deposition systems	668990-10G
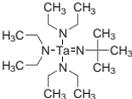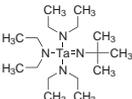
Zirconium

Name	Structure	Purity (%) and Grade	Prod. No.
Bis(cyclopentadienyl)zirconium(IV) dihydride		95	540692-1G
Dimethylbis(pentamethylcyclopentadienyl)zirconium (IV)		-	510793-5G
Tetrakis(diethylamido)zirconium(IV)		≥99.99	453153-5ML
Tetrakis(dimethylamido)zirconium(IV)		≥99.99	579211-5G
Tetrakis(dimethylamido)zirconium(IV)		-	445665-5G
Tetrakis(dimethylamido)zirconium(IV)		packaged for use in deposition systems	669016-25G
Tetrakis(ethylmethylamido)zirconium(IV)		≥99.99	553131-5G
Zirconium tetrakis(2,2,6,6-tetramethyl-3,5-heptanedionate)		≥99.99	478865-5G 478865-25G
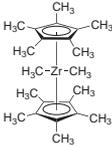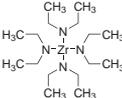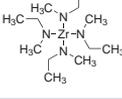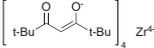
Crucibles for Research and Analysis
A Broad Range of Types, Sizes, and Accessories

Standard Form Platinum Crucibles

Cap. (mL)	Top × Bottom Diam. (mm)	Prod. No.
5	20.5 × 12	Z562238
10	26 × 15.5	Z562025
15	29 × 17.5	Z562041
25	41 × 25	Z562076
30	37.5 × 22.5	Z562092
50	49 × 30	Z562114

Coors™ High-Alumina Crucibles

Made of 99.8% pure, recrystallized aluminum oxide.
Max. use temp. (no load) 1,750 °C.

Cap. (mL)	Height (mm)	High Form Crucibles Prod. No.	Covers Prod. No.
20	35	Z247626	Z247723
50	47	Z247634	Z247731
100	61	Z247642	Z247758

Additional crucible types and accessories include:

- Inconel
- Nickel
- Zirconium
- Vycor
- Crucible Cradle™ (Z685151, shown at right)

For more information, visit
aldrich.com/crucibles

SIGMA-ALDRICH®

Low Resistivity Nanoscale Devices by Templated Electrochemistry

Mazin Maqableh, Madhukar Reddy (not pictured), Bethanie Stadler*
Department of Chemical Engineering and Materials Science,
University of Minnesota,
Minneapolis, Minnesota 55455, USA
*Email: stadler@umn.edu

Introduction

In many technologies, performance requirements drive device dimensions below the scale of electron mean free paths (λ_e). This trend has increased scientific interest and technological importance of electrical resistivities at the nanoscale.[1,16] Experimentally, transport properties have been measured in metallic nanostructures; however, contact design, corroded surfaces, grain boundary resistances, and scattering losses make measurements hard to interpret, especially for nanowires with exposed edges. Resistivity values can vary by several orders of magnitude for any given metal depending on fabrication and measurement techniques. Models of electron transport predict an order of magnitude higher resistivity for devices with 10 nm diameters due to sidewall scattering ($\lambda_{metals}\sim40$ nm), even if roughness is only one atomic spacing.[2] Enter templated electrochemically synthesized nanowires. Nearly bulk resistivities have been measured in 10 nm diameter metallic wires (200 nm long) that were synthesized inside anodic aluminum oxide (AAO) templates.[1] This article explores AAO templates, followed by nanowire synthesis and measurement techniques that can be used to elucidate intrinsic resistivities of nanoscale metals.

Templates with Negligible Sidewall Roughness

Two-step anodization of aluminum (either Al foil (Aldrich Prod. No. 266574) or Al films on Si) is the best process for synthesizing reproducible, very small nanopores with high aspect ratios.[3] This process involves applying a voltage to Al while it is submerged in either phosphoric (Aldrich Prod. No. 452289), oxalic (Aldrich Prod. No. 752835), or sulfuric acid (Aldrich Prod. No. 339741), depending on desired pore size. Although anodizing voltage has been the primary parameter used to reduce pore diameters from 250 down to 25 nm with a well-known linear dependence,[4] nanopore diameter can be independent of voltage at the smallest sizes (**Figure 1**, *page 42*). Therefore, to achieve smaller diameters, other parameters such as electrolyte dilution and temperature have been explored. For example, electrolyte dilution can be optimized to get diameters smaller than 10 nm, but careful monitoring of the thermal conditions is important. **Figure 1** shows scanning electron micrographs and histograms of nanopores made at different anodization voltages and electrolyte concentrations.[1]

Although these nanopores are excellent templates, nanowire devices discussed below can be electroplated into a variety nanoporous templates, including those being developed for bit patterned media (BPM).[5] This is important for mass production of read sensors, RAM, or 3D

nanoelectronics where long-range order will be necessary. Long-range order in alumina templates can be achieved by anodizing *nanoimprinted* Al,[6] for example 74 nm diameter pores are shown in **Figure 2**. Although very expensive, imprint stamps with 8 to 18 nm features have been made industrially via large-scale lithography, which means ordered and small pores will be possible.[7] It is important to note the expensive master stamps can be used to produce hundreds of wafers with 10^{12} electrochemically grown magnetic devices per square inch. In addition, daughter stamps from the e-beam masters can be produced in order to again multiply the number of sensors from each master by several orders of magnitude. Therefore, the cost per device will not be a barrier to implementation for industry, especially as e-beam lithography costs continue to decrease due to faster resists and writing software.
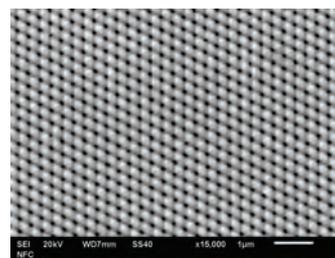
Figure 2. Nanoimprinted aluminum anodized using 160 V in 1% phosphoric acid at 0 °C. Pores in the resulting oxide self-assembled to align with imprints (74±10-nm diameters). Adapted from Reference 1.

Synthesis of Nanowires

Watts-type electrochemical baths are the most common electrolytes for synthesizing nanowires inside AAO nanopores. These contain sulfates of the metals of interest, and boric acid to maintain pH at the working electrode, if required. A metal contact film, such as Ti/Cu or Cr/Au, is sputtered or evaporated onto one side of the AAO. This side of the sample is then isolated such that only the open pores are exposed to the electrolyte. Unlike the anodization process, the electrochemical deposition process usually requires a reference electrode placed near the working electrode (in this case, the AAO pores).

Although electrochemical deposition is a fairly standard technique, many functional metals, such as magnetostrictive alloys, involve rare earths or Ga, which oxidize easily and are, therefore, challenging to electroplate.[8] For example, **Figure 3A** shows an Fe-Ga nanowire array grown under commonly employed conditions of agitation with a magnetic stirrer.[9] The wire lengths exhibit a bimodal distribution, with large relative standard deviation. In many applications precise multilayer thicknesses are required, so rotating disk electrodes (RDE) are employed to create uniform hydrodynamic conditions near the template surface to control wire lengths (**Figure 3B**). Initial layers, such as Cu, can also act as nucleation sites for subsequent alloy deposition (**Figure 3C**). Pulsed deposition is another technique in which rest periods ensure the absence of non-uniform overlapping of diffusion fields (**Figure 3D**).[10] In most cases, a combination of these strategies produces the most uniform results, as in FeGa nanowires shown in **Figure 3**.[9]
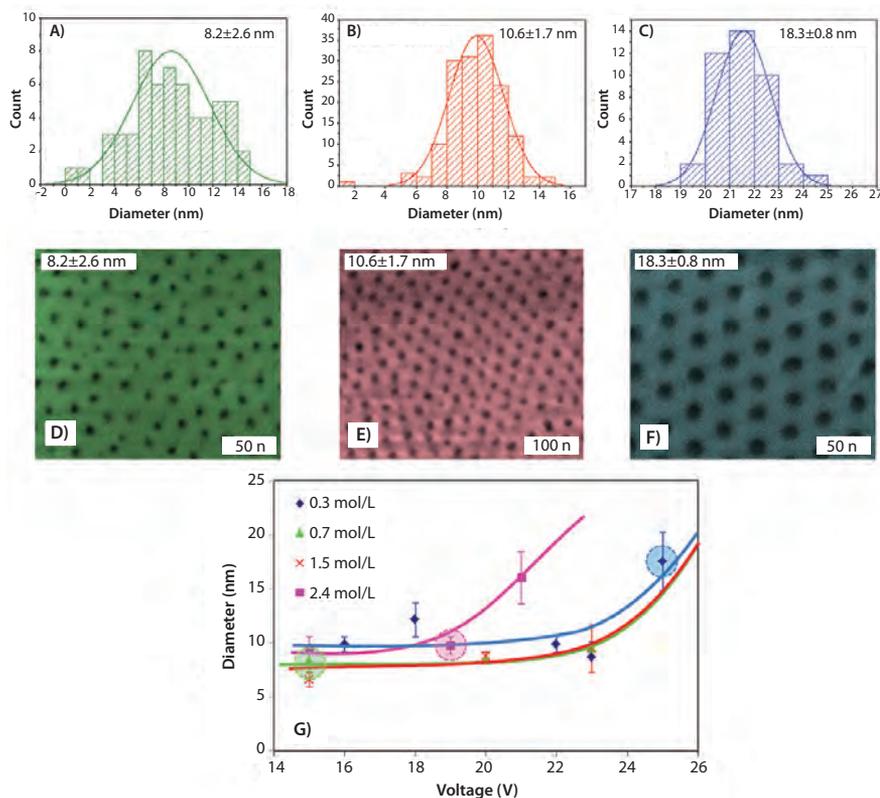
Figure 1. A–C) Diameter histograms of nanopores formed by anodization at various voltages and concentrations of H_2SO_4 at 1 °C, as shown in micrographs (D–F) and summarized in (G). Circled data points in (G) correspond to nanopores that were imaged using SEM as shown in the colored images. The pore size and distribution shown here were analyzed over large areas. Adapted from Reference 1.
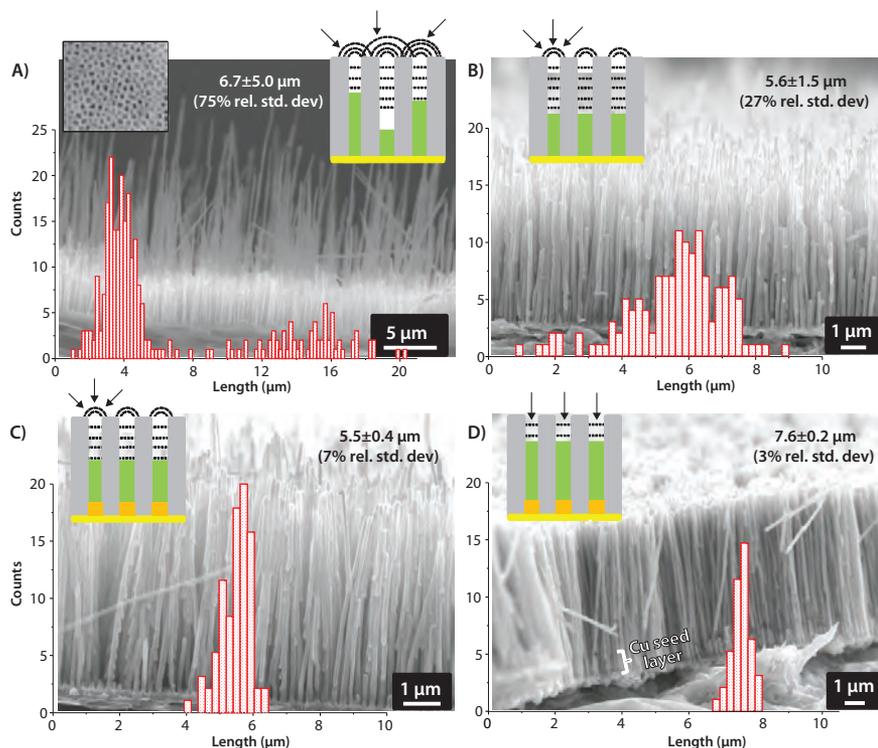
Figure 3. Optimization of Fe-Ga nanowire growths. Statistical analysis of nanowire lengths is superimposed on the corresponding SEM image. The schematics represent the diffusion profiles existing during growth in each case. A) Bimodal distribution obtained when the solution was agitated using a magnetic stirrer; B) after use of RDE-template at a rotation rate of 1,800 rpm; C) after use of Cu seed layer in addition to RDE-template; and D) use of pulse deposition in addition to Cu seed layer and RDE-template. Identical growth conditions including deposition potential, solution concentrations, and time of deposition were used. Adapted from Reference 9.

For questions, product data, or new product suggestions, contact Aldrich Materials Science at **matsci@sial.com**.

ALDRICH® Materials Science

43

Measuring Resistivity of 10 nm Nanowires

For statistical analysis of resistivities of 10 nm diameter nanowires, Au-coated AFM tips are used with various contact forces such that 1–3 wires are contacted.[11] A histogram of such resistance measurements for primarily copper nanowires is shown in **Figure 4**.[1] In the first ten measurements, single nanowires were contacted. All possible combinations of pairs of these 10 single nanowire measurements are shown next to the cluster of measurements in which 2 wires were contacted. Results for all 120 combinations of 3 single wires were compared to the next grouping of measured resistance values. These results indicate the first 10 measurements were those of single wires with resistances of 119.8±21.6 Ω. The average and distribution corresponds to 3.2 times the resistivity of bulk copper (ρ_o), or 5.4 μΩ·cm for the average diameter (10.6±1.7 nm) determined from micrographs such as **Figure 1B** using NIH freeware. The high resistance "tail" of the data shown in **Figure 4** is expected for an inverse Gaussian distribution that arises from resistances of nanowires with Gaussian distributions in diameters and, therefore, in areas (**Figure 1B**). This occurs due to the inverse relationship between resistance and area, R = ρ /A where was 190 nm for all of the wires.
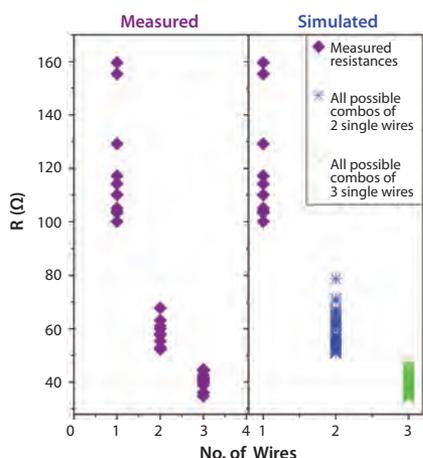
Figure 4. Resistance histogram of 10-nm nanowires measured (purple) while inside the AAO matrix. The measured groupings were separated by resistance gaps as 1, 2, or 3 wires were contacted. Blue points correspond to the 45 combinations of any two measurements of the individual nanowires. Green points correspond to all 120 possible combinations of any three individual nanowires. Adapted from Reference 1.

The International Technology Roadmap for Semiconductors (ITRS) has identified the "size effect" of increased resistivity (ρ) in nanostructures as a Grand Challenge to continued scaling of electronics. This increase in resistivity compared to bulk resistivity (ρ_o) is usually attributed to electron scattering from surfaces that can be approximated using the Fuchs-Sondheimer (FS) theory[12,13] for cylindrical wires:

$$\rho = \rho_o*[1 + \tfrac{3}{4}(1-p)\,\kappa] \tag{1}$$

where $\kappa = D/\lambda_e$, D is the wire diameter, λ_e is the mean free path of the electrons (39 nm for bulk Cu), and ρ is a constant (0-1) that depends on the type of electron reflection off the sample surfaces (from diffuse to specular). Most horizontally patterned nanowires from electroplated Cu films are even more resistive than this approximation predicts because grain boundaries etch preferentially, so the edges are rough after the nanowire is defined. Therefore, resistivities comparable to nanowires synthesized in AAO are only obtained with an order of magnitude larger cross sectional area.[14] Using the FS approximation, diffuse scattering at the sidewalls of 10 nm diameter nanowires predicts resistivities 19% higher than the measured resistivities of nanowires synthesized in AAO.

These resistances are higher than predicted by **Equation 1** because the approximation underestimates the size effect compared to exact solutions of the FS theory.[15] This result has also been confirmed analytically and numerically using an atomistic tight-binding approach where resistance (R) was calculated as a function of wire length to determine λ_e using

$$R = h/2e^2\,(1/M + 1/\lambda_e M) = h/2e^2\,(1/MT_{ave}) \tag{2}$$

where h and e are Planck's constant and electron charge, M is the number of conducting channels whose subbands cross the Fermi level, and T_{ave} is the average transmission probability.[2] This model predicted one atomic monolayer roughness would cause an order of magnitude higher resistivities for 10 nm diameter nanowires inside alumina compared to bulk. However, calculated resistivity is 200% higher than measured resistivities for AAO-template-synthesized nanowires, which leads us to conclude the AAO synthesized nanowires have very smooth sidewalls. Therefore, nanowires have great promise for device applications as low resistivity interconnects, random access memory,[17-29] and readheads.[20]

Conclusions

Templated electrochemistry allows the synthesis of nanodevices with very smooth sidewalls. This could provide a solution to the ITRS Grand Challenge calling for low resistivity interconnects at the nanoscale by mitigating the "size effect." In addition, devices in AAO templates can be synthesized in arrays with densities of 2 Tbit/in^2, a density usually reserved for hard drive media to date. Aspect ratios up to 10,000× are possible, which opens the possibility of better performance and even 3D devices. Given the extensive knowledge available for the synthesis of such devices, a wide range of applications should begin to emerge in the near future.

References

(1) Maqableh, M.; Huang, X.; Tan, L.; Victora, R.H.; Stadler, B.J.H., *Nano Letters*, **2012**, *12*, 4102.
(2) Chen, X.; Victora, R.H., *Appl. Phys. Letters*, **2008**, *93(16)*, 162105.
(3) Masuda, H.; Fukuda, K., *Science*, **1995**, *268*, 1466.
(4) Lee, W.; Ji, R.; Gösele, U.; Nielsch, K. Fast fabrication of long-range ordered porous alumina membranes by hard anodization. *Nat. Mater.* **2006**, 5, 741.
(5) Ross, C. A.; Cheng, J. Y., *MRS Bull.*, **2008**, *33*, 838.
(6) Zou, J.; Qi, X.; Tan, L.; Stadler, B.J.H., *Appl. Phys. Lett.*, **2006**, *89*, 093106.
(7) Yang, X.; Xiao, S.; Wu, W.; Xu, Y.; Mountfield, K.; Rottmayer, R.; Lee, K.; Kuo, D.; Weller, D., *J. Vac. Sci. Tech. B*, **2007**, *25*, 2202.
(8) Reddy, K.S.M.; Estrine, E.C.; Lim, D.-A.; Smyrl, W.H.; Stadler, B.J.H., *Electrochem. Comm.*, **2012**, *18*, 127.
(9) Reddy, K.S.M.; Park, J.J.; Na, S.-M.; Maqableh, M.M.; Flatau, A.B.; Stadler, B.J.H, *Adv. Funct. Mat.*, **2011**, *21*, 4677.
(10) Trahey, L.; Becker, C.R.; Stacy, A.M., *Nano Letters*, **2007**, *7*, 2535.
(11) Choi, D. S.; Rheem, Y.; Yoo, B.; Myung, N. V.; Kim, Y. K., *Curr. Appl. Phys.*, **2010**, *10*, 1037.
(12) Fuchs, K, Mathematical Proceedings of the Cambridge Philosophical Society, **1938**, 34, 100.
(13) Sondheimer, E. H., *Advances In Physics*, **1952**, *1*, 1.
(14) Kim, T.-H.; Zhang, X.-G.; Nicholson, D. M.; Evans, B. M.; Kulkarni, N. S.; Radhakrishnan, B.; Kenik, E. A.; Li, A.-P., *Nano Letters*, **2010**, *10(8)*, 3096.
(15) Steinhogl, W.; Schindler G.; Steinlesberger, G.; Engelhardt M., *Phys. Rev. B*, **2002**, *66*, 075414.
(16) McGary, P.D.; Tan, L.; Zou, J.; Stadler, B.J.H.; Downey, P.; Flatau, A., *J. Appl. Phys.*, **2006**, *99*, 08B310. Also selected for publication in the *Virtual Journal of Nanoscience & Technology* , **2006**, *13(18)*.
(17) Tan, L.; Stadler, B.J.H., *J. Mat. Research*, **2006**, *11*, 2870.
(18) Huang, X.; Tan, L.; Cho, H.; Stadler, B.J.H., *J. Appl. Phys*, **2009**, *103*, 07B504.
(19) Hernández, S.; Tan, L.; Stadler, B.J.H. Victora, R.H., *J. Appl. Phys.*, **2011**, *109*, 07C916.
(20) Maqablah, M.; Tan, L.; Huang, X.; Cobian, R.; Norby, G.; Victora, R.H., Stadler, B.J.H., *IEEE Trans. Magn.*, **2012**, *48*, 1.

Aluminum Foils

For a complete list of available materials, visit aldrich.com/pvd.

Name	Thickness	Purity (%)	Prod. No.
Aluminum	8 µm	99	733369-4EA
Aluminum	0.05 mm	99.8	356859-3.1G 356859-20.4G
Aluminum	0.13 mm	≥99.99	326860-900MG 326860-3.6G
Aluminum	0.25 mm	99.999	326852-1.7G 326852-6.8G
Aluminum	0.5 mm	99.999	266574-3.4G 266574-13.6G
Aluminum	1.0 mm	99.999	266957-27.2G

Acids for Anodization of Aluminum

For a complete list of available materials, visit aldrich.com/mnel.

Name	Composition	Purity (%) and Grade	Prod. No.
Oxalic acid	HO_2CCO_2H	99.999, purified grade	658537-25G 658537-100G
Oxalic acid	HO_2CCO_2H	≥99, *ReagentPlus*®	241172-50G
Oxalic acid	HO_2CCO_2H	98	194131-5G 194131-250G 194131-1KG
Phosphoric acid, ≥85 wt. % in H_2O	H_3PO_4	≥99.999	452289-50ML 452289-250ML
Phosphoric acid, 85 wt. % in H_2O	H_3PO_4	99.99	345245-100ML 345245-500ML
Phosphoric acid	H_3PO_4	semiconductor grade MOS PURANAL™ (Honeywell 17938)	40278-2.5L
Phosphoric acid	H_3PO_4	semiconductor grade PURANAL™ (Honeywell 17861)	40266-2.5L-R
Phosphoric acid	H_3PO_4	semiconductor grade VLSI PURANAL™ (Honeywell 17681)	40297-2.5L-R
Sulfuric acid	H_2SO_4	99.999	339741-100ML 339741-500ML 339741-6X500ML
Sulfuric acid	H_2SO_4	semiconductor grade VLSI PURANAL™ (Honeywell 17611)	40306-2.5L
Sulfuric acid	H_2SO_4	semiconductor grade PURANAL™ (Honeywell 17831)	40254-2.5L-R

Sulfates for Nanomaterial Deposition

For a complete list of available materials, visit aldrich.com/periodic.

Name	Composition	Purity (%)	Form	Prod. No.
Cadmium sulfate	$CdSO_4$	≥99.99 trace metals basis	solid	481882-5G 481882-25G
Cadmium sulfate hydrate	$CdSO_4 \cdot xH_2O$	99.999 trace metals basis	powder and chunks	202924-5G
Chromium(III) sulfate hydrate	$Cr_2(SO_4)_3 \cdot xH_2O$	99.999 trace metals basis	solid	455954-10G
Chromium(III) sulfate hydrate	$Cr_2(SO_4)_3 \cdot xH_2O$	-	solid	342432-100G 342432-500G
Cobalt(II) sulfate hydrate	$CoSO_4 \cdot xH_2O$	99.998 trace metals basis	crystals and lumps	229598-10G
Copper(II) sulfate	$CuSO_4$	≥99.99 trace metals basis	powder	451657-10G 451657-50G
Copper(II) sulfate pentahydrate	$CuSO_4 \cdot 5H_2O$	99.999 trace metals basis	crystals and lumps	203165-10G 203165-50G
Copper(II) sulfate pentahydrate	$CuSO_4 \cdot 5H_2O$	99.995 trace metals basis	crystalline	469130-50G 469130-250G
Iron(II) sulfate hydrate	$FeSO_4 \cdot xH_2O$	99.999 trace metals basis	solid	450278-5G 450278-25G
Nickel(II) sulfate	$NiSO_4$	99.99 trace metals basis	solid	656895-10G 656895-50G
Nickel(II) sulfate heptahydrate	$NiSO_4 \cdot 7H_2O$	99.999 trace metals basis	crystals and lumps	203890-10G 203890-50G 203890-250G
Nickel(II) sulfate hexa-/heptahydrate	$NiSO_4 \cdot 6\text{-}7H_2O$	≥20.6 Ni and Co basis	powder or crystals	13635-1KG-R 13635-6X1KG-R 13635-2.5KG-R 13635-6X2.5KG-R
Silver sulfate	Ag_2SO_4	99.999 trace metals basis	powder or crystals	204412-10G 204412-50G

For questions, product data, or new product suggestions, contact Aldrich Materials Science at matsci@sial.com.

ALDRICH® Materials Science

45

Name	Composition	Purity (%)	Form	Prod. No.
Tetraamminecopper(II) sulfate monohydrate	$Cu(NH_3)_4SO_4 \cdot H_2O$	98	powder and chunks	342327-5G
Titanium(IV) oxysulfate solution	$TiOSO_4$	99.99 trace metals basis	liquid	495379-250ML 495379-1L
Titanium(IV) oxysulfate - sulfuric acid hydrate	$TiOSO_4 \cdot xH_2SO_4 \cdot xH_2O$	99.99 trace metals basis	powder and chunks	463914-10G
Zinc sulfate heptahydrate	$ZnSO_4 \cdot 7H_2O$	99.999 trace metals basis	crystals and lumps	204986-10G 204986-50G 204986-250G
Zirconium(IV) sulfate hydrate	$Zr(SO_4)_2 \cdot xH_2O$	99.99 trace metals basis	solid	366773-25G 366773-125G
Zirconium(IV) sulfate solution	$Zr(SO_4)_2$	99.9 trace metals basis (purity excludes Hf)	liquid, 35 wt. % H_2O	520187-2L

One-dimensional Nanostructures

For a complete list of available materials, visit aldrich.com/nano.

Name	Composition	Dimensions (nm)	Form	Prod. No.
Zinc oxide	OZn	diam. × L 90 nm × 1 μm	nanowires	773999-500MG
Zinc oxide	OZn	diam. × L 50 nm × 300 μm	nanowires	773980-500MG
Zinc oxide	OZn	diam. × L 300 nm × 4-5 μm	nanowires	774006-500MG
Titanium(IV) oxide	O_2Ti	diam. × L ~100 nm × ~10 μm	nanowires	774510-500MG
Titanium(IV) oxide	O_2Ti	diam. × L ~10 nm × ~10 μm	nanowires	774529-500MG
Tungsten(VI) oxide	O_3W	diam. × L ~50 nm × ~10 μm	nanowires	774537-500MG
Nickel(II) oxide	NiO	diam. × L ~20 nm × ~10 μm	nanowires	774545-500MG
Gold nanorods	Au	diam. × L 10 × 38 ±10%	colloidal suspension dispersion in H_2O	716812-25ML
Gold nanorods	Au	diam. × L 10 × 41 ±10%	colloidal suspension dispersion in H_2O	716820-25ML
Gold nanorods	Au	diam. × L 10 × 45 ±10%	colloidal suspension dispersion in H_2O	716839-25ML
Gold nanorods, amine terminated	Au	diam. × L 10 × 41 ±10%	colloidal suspension dispersion in H_2O	716871-1ML
Gold nanorods, carboxyl terminated	Au	diam. × L 10 × 41 ±10%	colloidal suspension dispersion in H_2O	716898-1ML
Gold nanorods, methyl terminated	Au	diam. × L 10 × 41 ±10%	colloidal suspension dispersion in H_2O	716901-1ML
Gold nanorods, Pd coated	Au	diam. × L 25 × 75	colloidal suspension	716928-10ML
Gold nanorods, Pt coated	Au	diam. × L 25 × 75	colloidal suspension	716936-10ML
Gold nanorods	Au	diam. × L 25 × 60 (× ±10)	colloidal suspension dispersion in H_2O	771686-25ML
Gold nanorods	Au	diam. × L 25 × 47 (× ±10)	colloidal suspension dispersion in H_2O	771651-25ML
Gold nanorods	Au	diam. × L 25 nm × 34 nm (× ±10)	colloidal suspension dispersion in H_2O	771643-25ML
Gold nanowires	Au	diam. × L 30 × 4,500 diam. × L 30 × 4,500 ±20%	dispersion (H_2O)	716944-10ML
Gold nanowires	Au	diam. × L 30 × 6,000 ±20% diam. × L 30 × 6,000	dispersion (H_2O)	716952-10ML
Graphite	C	D × L 50-250 nm × 0.5-5 μm	powder	698830-1G
Silver nanowires	Ag	diam. × L 115 nm × 20-50 μm	liquid (suspension)	739448-25ML
Silver nanowires	Ag	diam. × L 60 nm × 10 μm	liquid (suspension)	739421-25ML

Functional Magnetic Materials: Synergy Between Basic Science and Evolving Technology

S. B. Roy
Materials and Advanced Accelerator Sciences Division
Raja Ramanna Centre for Advanced Technology
Indore-452013, India
Email: sbroy@rrcat.gov.in

Introduction

The application of magnetism and magnetic materials pervades our modern civilization in the form of electrical power, communications and information storage. The intensity and importance of such applications are reflected in the multi-billion dollar per year market for magnetic materials in three broad areas: hard magnets, soft magnets, and magnetic recording.[1] Continuous evolution in the field of magnetic materials has not, however, remained confined to these well-identified areas. Often classes of magnetic materials are discovered with interesting functionality, which stimulate the growth of new technology. In this article we discuss some such magnetic materials, where a solid-to-solid thermodynamic phase transition gives rise to interesting functional properties with futuristic applications.

Magnetic Materials with Phase Transition-driven Functionality

During the last two decades, three classes of magnetic materials have emerged with much promise for immediate technological applications. These are: 1) giant magneto-resistance materials; 2) magneto-strictive materials, including magnetic shape memory alloys; and 3) magneto-caloric materials.

The change in electrical resistance in a material with an applied magnetic field—commonly known as 'magneto-resistance'—finds applications in sensors in several areas of technology. For example, small personal computers now come outfitted with high capacity hard drives which use giant magneto-resistance (GMR) sensors as a read head. The basic GMR device consists of a three-layer sandwich of a magnetic metal such as cobalt or iron with a nonmagnetic metal filling such as silver or platinum.[2] The discovery of interesting GMR properties came as a bonus out of curiosity-driven scientific research to shed light on the fundamental question of magnetic interactions in materials; and from the first report in the mid-1980s it took less than ten years for the first product to arrive in the form of "read heads" for computer hard disk drives. This discovery naturally spurred more research activities, and in early 1990s a class of rare-earth manganese oxide materials (commonly termed as manganites) were identified with colossal magneto-resistance (CMR) properties.[3] Manganites show exotic physical properties in the form of a metal-insulator transition and a variety of magnetic, charge, and orbital ordering forms dictated by strong electron-electron interactions and electron-lattice interactions, provide a challenging area of research.

Shape memory alloys (SMA) are metals that can revert to a predetermined shape after any mechanical deformation.[4] The shape-memory effect is caused by a thermoelastic martensitic transition between two different crystal microstructures. SMAs started drawing much attention from the early 1960s with the discovery of shape-memory effect in nickel-titanium alloys,[4] and over time a number of commercial products came to the market. The conventional SMAs; however, have one drawback-they are relatively slow to respond to variations in temperature and the flow of heat. A class of materials known as magnetic shape-memory alloys (MSMA), discovered in the mid-1990s, can undergo large reversible deformations in an applied magnetic field.[5] The magnetic field control enables a relatively fast response in the MSMAs in comparison to the usual SMAs.

The magnetic field-induced isothermal entropy change or adiabatic temperature change in a magnetic solid is known as 'magneto-caloric effect' (MCE). Originally observed in iron in 1881, MCE offers the prospect of magnetic cooling technology, which has a potential to reduce global energy consumption and avoid the need of ozone depleting and greenhouse gas chemicals. In an MCE material, randomly oriented magnetic moments are aligned by an applied magnetic field in a magnetic-refrigeration cycle, resulting in reduction of magnetic entropy. In turn, the MCE material is heated via the increase of its lattice entropy. This heat is then removed from the material to its surroundings by a heat-transfer medium. On removing the magnetic field, the magnetic moments become randomized causing an increase in the magnetic entropy. This, in turn, leads to cooling of the MCE material below the ambient temperature. The prospect of magnetic cooling as a possible alternative to vapor-compression technology has increased enormously since the discovery of giant MCE in various classes of magnetic materials during last two decades.[6,7]

This article discusses certain common experimental features, which lead to interesting functional properties in these distinct types of magnetic materials–magneto-resistance materials, MSMAs, and giant MCE materials. A disorder-influenced first order phase transition provides the key to understanding and tuning the observed functional properties. Often all three functional properties are observed in the same material. This generality will be highlighted with the case study of a NiMnIn-based shape-memory alloy, which shows a large magneto-caloric effect, large magneto-resistance and large magneto-striction driven by a first order magneto-structural phase transition. A brief comparison is made with other classes of magnetic materials including giant magneto-caloric materials and CMR-manganites.

Phenomenology of First Order Phase Transition (FOPT)

FOPT is omnipresent in nature, with the classic example being boiling and freezing of water. The existence of FOPT involving a change in the lattice and/or spin degree of freedom in solid materials is also fairly well known. However, it is only during the last decade or so it has become apparent that the change in the magnetic and lattice structure associated with such FOPT in a material can actually give rise to interesting functional properties of technological importance.

For questions, product data, or new product suggestions, contact Aldrich Materials Science at matsci@sial.com.

ALDRICH® Materials Science

47
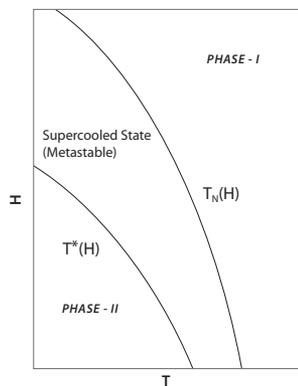
Figure 1. Schematic (H,T) phase diagram showing the phase transition line $T_N(H)$ and the stability limit $T^*(H)$ for the supercooled state.

In a magnetic solid, an FOPT is identified across a $T_N(H)$ (here T_N is the phase transition temperature) line in the two-parameter magnetic field (H)-temperature (T) phase space (**Figure 1**), by a discontinuous change in entropy (i.e., measureable latent heat) or a discontinuous change in magnetization (M) as this $T_N(H)$ line is crossed by varying either of the control variables T or H. The high- and low-temperature phases coexist at the transition temperature $T=T_N$, and the high temperature phase continues to exist as a supercooled metastable state until the temperature T^*.[8] The limit of metastability (superheating) while heating is reached at $T^{**}(H)>T_N(H)$, and this is not shown in the schematic (H,T) phase diagram (**Figure 1**) for the sake of clarity. In a similar way the limits of metastability H^* and H^{**} can be defined across an isothermal magnetic field-induced FOPT.

The functional magnetic materials of present interest are mostly multi-component alloys and chemical compounds, where the actual composition varies around some average composition due to disorder that is frozen in as the solid crystallizes from the melt. In a pioneering work, Imry and Wortis[9] showed that such static, quenched-in, purely statistical compositional disorder would introduce a landscape of transition temperatures in a system undergoing FOPT. In addition, disorder will also cause a phase-coexistence of equilibrium and metastable phases associated with supercooling/superheating in the H-T region encompassed by $T_N - T^*(T^{**})$ lines. Such phase coexistence gives rise to hysteretic behavior in an observable property across an FOPT. While thermodynamic properties are the most commonly measured other physical properties can also display hysteretic behavior.[10]

$Ni_{50}Mn_{34}In_{16}$ Heusler Alloy: A Representative Multifunctional Material

$Ni_{50}Mn_{34}In_{16}$ belongs to the same family of Heusler alloys as that of the well-known magnetic shape-memory alloy Ni_2MnGa, which undergo a martensitic transition (an FOPT) from high-temperature austenite phase to low-temperature martensite phase. These Heusler alloys have an $L2_1$ cubic crystal structure in the austenite state, with different types of structure possible in the martensite state, the most prevalent one being the tetragonal $L1_0$ structure.
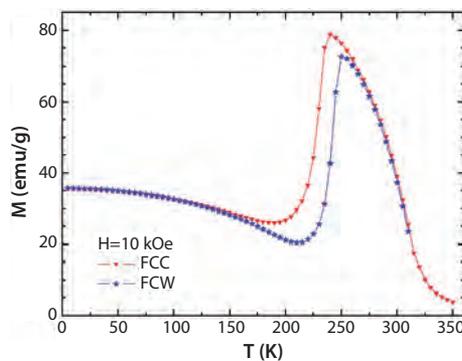
Figure 2. Magnetization (M) versus temperature (T) plot for $Ni_{50}Mn_{34}In_{16}$ alloy obtained while cooling in a magnetic field of 10 kOe (FCC mode) and warming in the same field (FCW mode).[11]

Figure 2 presents a magnetization (M) versus temperature (T) plot for the $Ni_{50}Mn_{34}In_{16}$ alloy, which exemplifies the large change in magnetization across the martensitic transition taking place around 240 K.[11] A distinct thermal hysteresis is observed in the phase transition temperature region, which highlights the first order nature of this transition.[11] A magnetic field-induced transition from a low magnetization martensite state to a higher magnetization austenite state is observed in the low temperature region in many off-stoichiometric compositions of Ni_2MnIn Heusler alloys, including the present $Ni_{50}Mn_{34}In_{16}$ alloy. The typical isothermal M-H curves showing magnetic field-induced martensite to austenite phase transition are presented in **Figure 3**. The various characteristic features of such M-H curves can be explained within the framework of a disorder-broadened FOPT.[11]
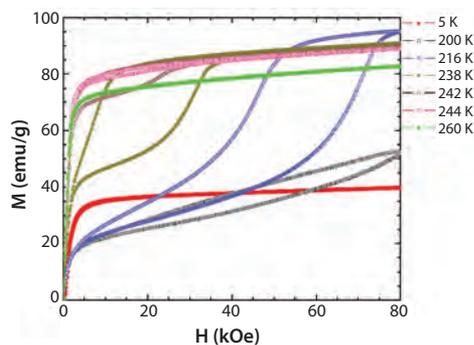
Figure 3. Isothermal magnetization (M) versus field (H) curves of $Ni_{50}Mn_{34}In_{16}$ alloy at representative temperatures.[15] The M-H curves at T=200 K, 216 K, 238 K, 242 K, and 244 K show the signature of a field-induced transition from martensite to austenite phase.[11]

Scanning Hall-probe imaging experiments have been performed across the magnetic field-induced martensite to austenite phase transition in the $Ni_{50}Mn_{34}In_{16}$ alloy; these provide snapshots of the coexistence of the martensite phase (with a low value of magnetization) and the austenite phase (with a high value of magnetization) on a length scale of tens of micrometers, extended over a wide magnetic field regime.[12] Furthermore, the characteristics exhibited by the local Hall voltage loops indicated the presence of a landscape of critical magnetic fields for the martensitic phase transition across the sample confirming this magnetic field-induced FOPT in the $Ni_{50}Mn_{34}In_{16}$ alloy is influenced by disorder. This kind of disorder-induced landscape of transition temperatures or magnetic fields[9] along with phase-coexistence and metastability had previously been observed in doped-$CeFe_2$ alloys (which belong to the same family as that of the well-known commercial magneto-strictive material Terfenol-$(Tb,Dy)Fe_2$ with multifunctional properties.[13]

The observed large drop in magnetization across the FOPT in the $Ni_{50}Mn_{34}In_{16}$ alloy (see **Figure 2**) and the magnetic field dependence of the transition temperature lead to a large isothermal entropy change of about 18 J/kg-K for a magnetic field variation of 50 kOe.[14] Similar large

magneto-caloric effects (MCE) associated with the FOPT have been observed in other compositions of Ni-Mn-In Huesler alloys.[15] Magnetic and structural inhomogeneities in the phase-coexistence regime are at the root of the observed large MCE. It is now recognized that lattice-entropy change accounts for about one half of the total entropy change in such NiMnIn alloys; and this, in turn, points to the important role of magneto-structural coupling.[16] The same temperature- and magnetic-field induced FOPT also gave rise to GMR[17] and superelasticity[18] in the $Ni_{50}Mn_{34}In_{16}$ alloy. The martensitic transition temperature of $Ni_{50}Mn_{34}In_{16}$, along with the functional properties, can be shifted towards room temperature with Cr-doping at Mn sites and Cu-doping at the Ni sites.[19] **Figures 4-6** present examples of multifunctional properties in a 1% Cu-doped $Ni_{50}Mn_{34}In_{16}$ near room temperature.
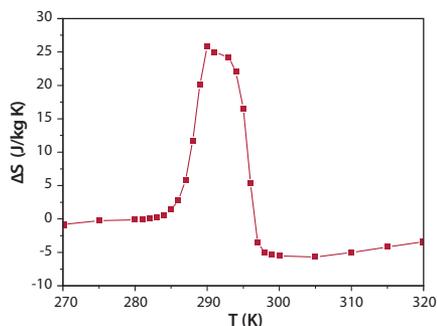
Figure 4. MCE (represented by isothermal entropy change) versus temperature plot in 1% Cu-doped $Ni_{50}Mn_{34}In_{16}$ alloy for a magnetic field variation of 45 kOe.[19]
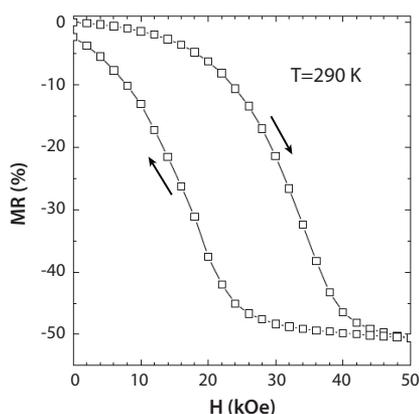
Figure 5. Isothermal magneto-resistance as a function of magnetic field in 1% Cu-doped $Ni_{50}Mn_{34}In_{16}$ alloy at T=290 K.[19]
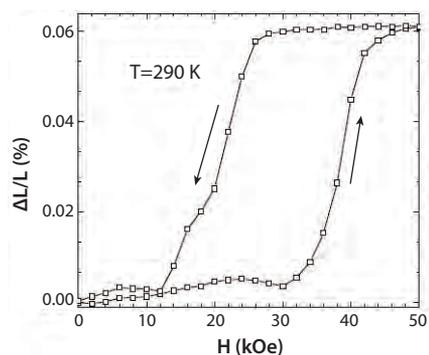
Figure 6. Isothermal strain as a function of magnetic field in 1% Cu-doped $Ni_{50}Mn_{34}In_{16}$ alloy at T=290 K.[19]

Commonality with other Multifunctional Materials

The thermomagnetic hysteresis, phase-coexistence, and metastability discussed above for $Ni_{50}Mn_{34}In_{16}$ are the characteristic features of a disorder-influenced FOPT and have been observed in various other classes of functional magnetic materials. We present below a brief discussion on the giant MCE material Gd_5Ge_4, CMR-manganites and equi-atomic FeRh alloys to highlight the role of disorder-influenced FOPT in the multifunctional properties of these materials. The generality of this observation can be extended to many other materials, including $LaFe_{13-x}Si_x$ and $MnCoGeB_x$, but a detailed discussion is beyond the scope of this article.

The parent compound Gd_5Ge_4 undergoes a low temperature first order antiferromagnetic (AFM)-to-ferromagnetic (FM) transition in the presence of an applied magnetic field. Thermomagnetic hysteresis is one of the numerous evidences pointing toward the first order nature of this AFM-FM phase transition in Gd_5Ge_4.[10] Scanning micro-Hall probe technique has been used to image the AFM-FM transition in Gd_5Ge_4, and revealed the coexistence of FM and AFM phase in micrometer scale in a finite H-T regime around the first order phase transition line showing the validity of a T_N/H_M landscape picture in Gd_5Ge_4.[10] In combination with dimensional analysis and numerical simulation, these results further pointed out how this AFM-FM phase-coexistence and the associated dynamics (nucleation and growth) could provide useful information for tuning the functional properties of Gd_5Ge_4.

The unique layered structure of Gd_5Ge_4 is at the root of the observed temperature and magnetic field-induced first order structural transition from a monoclinic-paramagnetic to an orthorhombic-ferromagnetic structure in these alloys, which in turn gives rise to giant MCE.[20] The first order AFM-FM transition in Gd_5Ge_4 is also accompanied by magneto-elastic effect, which gives rise to large magneto-striction[21] and magneto-resistance.[22]

A first order phase transition from a metallic FM state to an insulating charge-ordered AFM state in $La_{0.5}Ca_{0.5}MnO_3$, marked by sharp drop in M (T) and change in the resistivity (ρ) by several orders of magnitude, was reported in one of the earliest works on CMR-manganites.[23] A distinct thermal hysteresis was observed in both M(T) and ρ(T) in the phase transition region, and this was taken as a signature of the FOPT.[24] A drastic change of lattice constants was also observed in the vicinity of the AFM-FM transition in $La_{0.5}Ca_{0.5}MnO_3$.[24] Kuwahara et al. reported a similar first-order FM-AFM transition in $Nd_{0.5}Sr_{0.5}MnO_3$.[25] An AFM-FM transformation could be induced inside the AFM state with the application of an external magnetic field, and was clearly marked with sharp changes in physical properties and the accompanying hysteresis.[25] A percolation path involving the metallic FM phase in the phase-coexistence regime across the AFM-FM transition, which could be manipulated by an applied H, was proposed as a promising framework to explain the colossal magneto-resistance observed in the manganites.[3] Subsequently, the existence of this percolative conducting path in the phase transition region has been confirmed experimentally,[26] and a distinct phase-coexistence on a micrometer scale has been observed.[27,28] A substantial magneto-caloric effect (MCE) associated with the first order AFM-FM transition has been reported in several CMR-manganites.[6,29] The magnetic field-induced change in the configurational entropy associated with the structural transition and the magnetic inhomogeneity arising from the AFM-FM phase-coexistence across the disorder-influenced AFM-FM FOPT, are responsible for the large observed MCE. The commonality in the various features associated with the H- and T-induced first order AFM-FM transition in CMR manganites systems, giant magneto-caloric materials $Gd(Ge,Si)_4$, and doped -$CeFe_2$ alloys has been previously highlighted.[10]

Another system of interest is the equi-atomic FeRh alloy, which forms in the cubic CsCl-type structure and undergoes a first order phase transition from an FM to an AFM state around 330 K. This FOPT in the FeRh alloy gives rise to GMR, giant MCE, giant elastocaloric effect and giant magneto-striction close to room temperature. Thermomagnetic history effects, phase coexistence and the landscape of transition temperatures associated with the FOPT in Fe-Rh alloy have been studied in detail through magnetization, magnetic force microscopy, and linear strain measurements.[30-32] It has been shown that an MCE of about 12 J/kg-K reproducible under multiple field cycles could be achieved in FeRh-based alloys by properly choosing a combination of isothermal and adiabatic field variation cycles in the H-T phase space.[31]

Table 1 presents a comparison of first order phase transition-driven magneto-caloric effects in various classes of magnetic materials discussed above. The temperature T where isothermal entropy change attains its maximum value $|\Delta S_{max}|$, usually coincides with the first order phase transition temperature of the material concerned.

Table 1. Comparative Magneto-caloric Properties of Common MCE Materials

Materials	First Order Phase Transition Temp. (K)	Change in Magnetic Field (kOe)	Isothermal Entropy Change $|\Delta S_{max}|$ (J/kg-K)	Ref.
$Ni_{50}Mn_{34}In_{16}$	240	50	17	14
$Ni_{50}(Mn,2\%Cr)_{34}In_{16}$	294	50	24.4	12
$(Ni,2\%Cu)_{50}Mn_{34}In_{16}$	192	45	25.8	19
Gd_5Ge_4	40	50	25	6
$Gd_5Ge_2Si_2$	272	50	36	6
$Pr_{0.5}Sr_{0.5}MnO_3$	161	10	7.1	6
$Nd_{0.5}Sr_{0.5}MnO_3$	183	10	7.57	6
FeRh	300	50	12	13

Interdisciplinary Research Gains

The interesting features associated with an FOPT play important roles in a wide variety of real-life phenomena like the formation of rain clouds, the supercooling of fish blood, the survival of trees in the arctic region, and the formation of metallic alloys.[33] Scientific research on functional magnetic materials can also help in the deeper understanding of such FOPT processes in general. Such materials can actually be used as test bed materials to study an FOPT process in a two-parameter H-T phase space. Knowledge gathered in exploring the H-T phase space in magnetic materials can be applied in other areas of technological interest, including vortex matter phases of type-II superconductors and ferroelectric materials. While implications in ferroelectric materials are well known, the understanding of vortex matter phase space will be useful for tuning the dissipationless current-carrying capacity of a type-II superconductor.

Some liquids called "glass formers" experience a viscous retardation of nucleation and crystallization in their supercooled state and, instead of undergoing a liquid-solid phase transition, they enter into a glassy state. The nature of this glass transition is considered to be one of the important unsolved problems in condensed matter physics.[34] It has been observed that in certain regions of the H-T phase diagrams of the different functional magnetic materials ($CeFe_2$-based alloys, Gd_5Ge_4, CMR-manganites, NiMnIn Heusler alloys and RhFe discussed in sections above) there is a viscous retardation of nucleation and growth of the low-temperature phase across the FOPT.[10] The low-temperature state attains a configuration consisting of a fraction of transformed low-T equilibrium phase (e.g., AFM in doped $CeFe_2$ alloys and FeRh, and FM in Gd_5Ge_4) distributed randomly in an untransformed non-equilibrium matrix of the high-T phase (e.g., FM in doped $CeFe_2$ alloys and FeRh, and AFM in Gd_5Ge_4), and this configuration is frozen in time. The onset of

this non-trivial low temperature glass-like non-equilibrium state is marked by characteristic dynamic features, which are usually considered to be the hallmark of a structural glass transformation.[10] This non-equilibrium state is given the name "magnetic-glass,"[35] which is distinctly different from a conventional spin-glass state, where the spin configuration is frozen at random on a much shorter microscopic scale; or from a spin-ice state, where disorder of the magnetic moments at low temperatures is analogous to the proton disorder in water ice.[36] Easy accessibility of the experimental H-T phase space of such magnetic materials may provide opportunities for deeper studies of kinetic arrest of an FOPT leading to a glass-like state. In contrast, similar exploration in a more conventional pressure-temperature phase space is relatively difficult. Only very recently has it been discovered that liquid germanium can undergo a glassy transition in the presence of applied pressure.[37]

Future Outlook

In summary, a first order magneto-structural transition is a common phenomenon observed in many classes of functional magnetic materials of current interest, independent of the nature of their microscopic magnetic interactions. The coupling between spin and lattice degree of freedom is an important ingredient in this temperature and magnetic field-induced transition. Phase-coexistence and metastability are the characteristic features of the transition process and they influence the functionalities observed in the materials. Understanding these phenomena in detail will help tune the multifunctional properties of the existing materials as well as find new materials with improved functionality. The utility of CMR-manganite materials and shape-memory Heusler alloys as potential MCE materials in future magnetic cooling technology has also been recognized. It is clear the stronger the MCE the higher the efficiency of a magnetic refrigerator will be and, in this direction, materials with first order magneto-structural phase transition will play an important role. With the improvements in magnetic materials, magnet systems, and understanding of the active magnetic regenerator cycle, there is promise that mature, environmentally friendly magnetic refrigeration technology will soon produce thermodynamic efficiencies comparable to or higher than the best available gas compression devices.

References
(1)   Coey, J.M.D., *J. Magn. Magn. Mater.*, **2001**, *226-230*, 2107.
(2)   Prinz, G., *Science*, **1998**, *282* ,1660.
(3)   Dagotto, E., Nanoscale Phase Separation and Colossal Magneto-resistance, (Springer, 2002).
(4)   Otsuka, K.; Wayman, C.M., eds., Shape Memory Materials (Cambridge University Press, Cambridge), 1998.
(5)   Gerstner E., Materials Update (Nature Publishing Group), October 2002.
(6)   Gschneidner Jr., K.A.; Pecharsky, V.K.; Tsokol, A.O., *Reports on Progress in Physics*, **2005**, *68(6)*, 1479.
(7)   Gschneidner Jr., K.A.; Mudryk, Y.; Pecharsky, V.K., *Scripta Materialia*, **2012** *67(6)*, 572-577.
(8)   Chaikin, P.M.; Lubensky, T.C., Principles of Condensed Matter Physics, (Cambridge University Press, 1995).
(9)   Imry, Y.; Wortis, M., *Phys. Rev. B*, **1979**, *19*, 3580.
(10) Roy, S.B.; Chaddah, P.; Pecharsky, V.K.; Gschneidner Jr., K.A., *Acta Materialia*, **2008**, *56*, 5895.
(11) Sharma, V.K.; Chattopadhyay, M.K.; Roy, S.B., *J. Phys.: Condens. Matter*, **2008**, *20*, 425210.
(12) Sharma, V.K.; Moore, J.D.; Chattopadhyay, M.K.; Morrison, K.; Cohen, L.F.; Roy, S.B., *J. Phys.: Condens. Matter*, **2008**, *22*, 016008.
(13) Roy, S.B.; Perkins, G.K.; Chattopadhyay, M.K.; Sokhey, K.J.S.; Nigam, A.K.; Chaddah, P.; Caplin, A.D.; Cohen, L.F., *Phys. Rev. Lett.*, **2004**, *92*, 147203.
(14) Sharma, V.K.; Chattopadhyay, M.K. and Roy, S.B., *J. Phys. D: Appl. Phys.*, **2007**,*40* ,1869.
(15) Planes, A., *J. Phys.: Condens. Matter*, **2009**, *21(23)*, 233201.
(16) Li, B.; Ren, W.J.; Zhang, Q.; Lv, X.V.; Liu, X.G.; Meng, H.; Li, J.; Li, D.; Zhang, Z.D., *Appl. Phys. Lett.*, **2009**, *95*, 172506.
(17) Sharma, V.K.; Chattopadhyay, M.K.; Shaeb, K.H.B.; Chouhan, A.; Roy, S.B., *Appl. Phys. Lett.*, **2006**, *89*, 222509.

(18) Krenke, T.; Duman, E.; Acet, M.; Wassermann, E.F.; Moya, X.; Manosa, L.; Planes, A.; Suard, E.; Ouladdiaf, B., *Phys. Rev. B*, **2007**, *75*, 104414.
(19) Sharma, V.K.; Chattopadhyay, M.K.; Khandelwal, A.; Roy, S.B., *Phys. Rev. B*, **2010**, *82*, 172411.
(20) Pecharsky, V.K.; Holm, A.P.; Gschneidner Jr., K.A.; Rink, R., *Phys. Rev. Lett.*, **2003**, *91(19)*, 197204.
(21) Magen, C.; Morellon, L.; Algarabel, P.A.; Marquina, C.; Ibarra, M.R., *J. Phys.: Condens. Matter*, **2003**, *15*, 2389.
(22) Levin, E.M.; Pecharsky, V.K.; Gschneidner Jr., K.A.; Miller, G.J., *Phys Rev B*, **2001**, *64*, 235108.
(23) Schiffer, P.; Ramirez, A.; Bao, O.; Cheong, S.W., *Phys. Rev. Lett.*, **1995**, *75*, 3336.
(24) Radaeli P.G.; Cox, D.E.; Marezio, M.; Cheon, S.-W.; Schiffer, P.; Ramirez, A.P., *Phys. Rev. Lett.*, **1995**, *75*, 4488.
(25) Kuwahara, H.; Tomioka, Y.; Asamitsu, A.; Moritomo, Y.; Tokura, Y., *Science*, **1995**, *270*, 961.

(26) Zhang, L.; Israel, C.; Biswas, A.; Greene, R.; Lozanne, A., *Science*, **2002**, *298*, 805.
(27) Loudon, J.C.; Mathur, N.D.; Midgley, P.A., *Nature*, **2002**, *420*, 797.
(28) Murakami, Y.; Yoo, J.H.; Shindo, D.; Atou, T.; Kikuchi, M., Nature, **2003**, *423*, 965.
(29) Phan, M.H.; Yu, S.C., *J. Magn. Magn. Mater.*, **2007**, *308*, 325.
(30) Manekar, M.A.; Mukherjee, C.; Roy, S.B., *Euro Phys. Lett*, **2007**, *80*, 17004.
(31) Manekar, M.A.; Roy, S.B., *J. Phys. D: Appl. Phys.*, **2008**, *41*, 192004.
(32) Manekar, M.; Sharma, V.K.; Roy, S.B., *J. Phys.: Condens. Matter*, **2012**, *24*, 216004.
(33) Heneghan, A.F.; Wilson, P.W.; Haymet, A.D.J., *PNAS*, **2002**, *99*, 9631.
(34) Anderson, P. W., *Science*, **1995**, *267*, 1615.
(35) Chattopadhyay, M.K.; Roy, S.B.; Chaddah, P., *Phys. Rev.*, **2005**, *B72*, 180401(R).
(36) Roy, S.B.; Chattopadhyay, M.K., *Phys. Rev.*, **2009**, *B79*, 052407.
(37) Bhat, M.H.; Molinero, V.; Soignard, E.; Solomon, V.C.; Sastry, S.; Yarger, J.L., *Nature*, **2007**, *448*, 787.

Magnetic Alloys

For a complete list of available materials, visit aldrich.com/magnetic.

Name	Composition	Form	Thickness × Diam. (mm)	Prod. No.
Samarium-cobalt alloy 24	Sm_2Co_{17}	disc	10 × 6	692840-3EA
Samarium-cobalt alloy 18	$SmCo_5$	disc	10 × 6	692859-3EA
Aluminum nickel cobalt	Al / Ni / Co	disc	13 × 6	692867-2EA
Aluminum nickel cobalt	Al / Ni / Co	disc	13 × 6	692875-3EA
Aluminum nickel cobalt	Al / Ni / Co	disc	13 × 6	692883-3EA
Neodymium-iron-boron alloy 30/150	Nd \ Fe \ B	disc	13 × 6	693782-3EA
Neodymium-iron-boron, alloy 30/100	Nd \ Fe \ B	disc	13 × 6	693790-5EA
Neodymium-iron-boron, alloy 30/200	Nd \ Fe \ B	disc	13 × 6	693820-3EA
Samarium cobalt	Sm_2Co_7	powder	-	339229-50G

Rare-earth Metals

For a complete list of available materials, visit aldrich.com/periodic.

Name	Composition	Purity (%)	Form	Prod. No.
Cerium	Ce	99.9	chips chunks	461210-50G
Cerium	Ce	99.9	ingot	261041-25G 261041-100G
Dysprosium	Dy	99.9	chips	263028-5G 263028-25G
Dysprosium	Dy	99.9 (REM)	foil	693707-1EA
Dysprosium	Dy	99.9	ingot	261076-10G
Erbium	Er	99.9	chips	263052-10G
Erbium	Er	99.9 (REM)	foil	693685-1EA
Erbium	Er	99.9	ingot	261084-10G
Erbium	Er	99.95	dendritic pieces	755990-1G
Europium	Eu	-	chip (in mineral oil)	457965-5G
Europium	Eu	99.9	ingot	261092-1G
Gadolinium	Gd	99.99 (REM)	ingot	691771-10G
Holmium	Ho	99.9	chips	457957-5G
Holmium	Ho	99.9 (REM)	foil	693693-1EA
Holmium	Ho	99.99	dendritic pieces	755974-1G
Lanthanum	La	99.9	ingot (under oil)	261130-25G
Lanthanum	La	99.9	pieces	263117-25G
Lutetium	Lu	99.9	ingot	261149-1G
Lutetium	Lu	99.9 (REM)	foil	693650-1EA
Lutetium	Lu	99.99	dendritic pieces	755982-1G

For questions, product data, or new product suggestions, contact Aldrich Materials Science at matsci@sial.com.

ALDRICH Materials Science

51

Name	Composition	Purity (%)	Form	Prod. No.
Neodymium	Nd	99.9	chips	263141-25G 263141-100G
Neodymium	Nd	99.9 (REM)	foil	693758-1EA
Neodymium	Nd	99.9	ingot (in mineral oil)	261157-25G
Praseodymium	Pr	99.9	ingot	261173-10G
Samarium	Sm	99.9	chips	261211-10G
Samarium	Sm	99.9 (REM)	foil	693731-1EA
Samarium	Sm	99.9	ingot	263184-10G
Samarium	Sm	99	(powder or filings)	261203-1G 261203-10G 261203-50G
Scandium	Sc	99.9	dendritic pieces	261246-1G
Terbium	Tb	99.9	chips	263206-1G 263206-5G
Terbium	Tb	99.9 (REO)	foil	693715-1EA
Thulium	Tm	99.9	chips	262978-1G
Ytterbium	Yb	99.9	chips	262986-5G
Ytterbium	Yb	99.9	chunks	548804-5G
Ytterbium	Yb	99.9 (rare earth)	foil	693669-1EA
Ytterbium	Yb	99.9	ingot	261300-5G
Yttrium	Y	99.9	chips	262994-5G 262994-25G
Yttrium	Y	99.9	dendritic pieces	451347-1G
Yttrium	Y	99.9 (REO)	foil	693642-1EA
Yttrium	Y	99.9	ingot	261319-10G 261319-50G

Magnetic Nanomaterials

For a complete list of available materials, visit aldrich.com/nanomagnetic.

Name	Composition	Purity (%)	Particle Size	Form	Prod. No.
Barium ferrite	$BaFe_{12}O_{19}$	>97	particle size <100 nm (BET)	nanopowder	637602-25G
Cobalt	Co	≥99	particle size <50 nm (TEM)	nanopowder	697745-500MG
Cobalt aluminum oxide	$CoAl_2O_4$	≥99 (BET)	particle size <50 nm (BET)	nanopowder	633631-25G
Cobalt iron oxide	$CoFe_2O_4$	99	particle size 30 mm (TEM)	nanopowder	773352-5G
Cobalt(II,III) oxide	Co_3O_4	99.5	particle size <50 nm (TEM)	nanopowder	637025-25G 637025-100G 637025-250G
Copper iron oxide	$CuFe_2O_4$	98.5	particle size <100 nm (BET)	nanopowder	641723-10G
Copper zinc iron oxide	$CuZnFe_2O_4$	98.5	particle size <100 nm (BET)	nanopowder	641650-10G 641650-50G
Dysprosium(III) oxide	Dy_2O_3	≥99.9	particle size <100 nm (BET)	nanopowder	637289-25G
Dysprosium(III) oxide	Dy_2O_3	≥99.9	particle size <100 nm (BET)	dispersion	639664-25ML
Holmium(III) oxide	Ho_2O_3	≥99.9	particle size <100 nm (BET)	dispersion	641863-25ML
Holmium(III) oxide	Ho_2O_3	≥99.9	avg. part. size <100 nm (DLS)	nanopowder	637327-10G 637327-50G
Iron nickel oxide	Fe_2O_3/NiO	≥98	particle size <50 nm (APS)	nanopowder	637149-25G 637149-100G
Iron(II,III) oxide	Fe_3O_4	≥98	particle size <50 nm (TEM)	nanopowder spherical	637106-25G 637106-100G 637106-250G
Iron(III) oxide	Fe_2O_3	-	particle size <50 nm (BET)	nanopowder	544884-5G 544884-25G
Nickel	Ni	≥99	particle size <100 nm	nanopowder	577995-5G
Nickel(II) oxide	NiO	99.8	particle size <50 nm (TEM)	nanopowder	637130-25G 637130-100G 637130-250G

Name	Composition	Purity (%)	Particle Size	Form	Prod. No.
Nickel zinc iron oxide	$NiZnFe_2O_4$	≥99	particle size <100 nm (BET)	nanopowder	641669-10G 641669-50G
Strontium ferrite	$SrFe_{12}O_{19}$	99.8	particle size <50 nm (XRD)	crystalline (hexagonal phase) nanopowder	633836-5G
Yttrium iron oxide	$Y_3Fe_5O_{12}$	99.9	particle size <100 nm (BET)	nanopowder	634417-10G
Zinc iron oxide	$ZnFe_2O_4$	>99	particle size <100 nm (BET)	nanopowder	633844-10G 633844-50G

Iron Oxide Nanoparticle Dispersions

For a complete list of available materials, visit aldrich.com/nanomagnetic.

Name	Concentration	Avg. Part. Size (nm)	Prod. No.
Iron oxide(II,III), magnetic nanoparticles solution	5 mg/mL in toluene	10	700312-5ML
Iron oxide(II,III), magnetic nanoparticles solution	5 mg/mL in toluene	5	700320-5ML
Iron oxide(II,III), magnetic nanoparticles solution	5 mg/mL in toluene	20	700304-5ML
Iron oxide(II,III), magnetic nanoparticles solution	5 mg/mL in H_2O	10	725358-5ML
Iron oxide(II,III), magnetic nanoparticles solution	5 mg/mL in H_2O	20	725366-5ML
Iron(III) oxide, dispersion	20 wt. % in ethanol	<30 (APS)	720712-100G
Iron(III) oxide, dispersion	20 wt. % in H_2O	<30 (APS)	720704-100G
Iron oxide(II,III), magnetic nanoparticles solution	5 mg/mL in H_2O	5	725331-5ML

Rare-earth Solution Deposition Precursors

For a complete list of available materials, visit aldrich.com/mnel.

Name	Composition	Purity (%)	Form	Prod. No.
Cerium(III) acetate hydrate	$Ce(CH_3CO_2)_3 \cdot xH_2O$	99.99	powder or crystals	529559-10G
Cerium(III) acetate hydrate	$Ce(CH_3CO_2)_3 \cdot xH_2O$	99.9	powder and chunks	367753-50G 367753-250G
Cerium(III) acetylacetonate hydrate	$Ce(C_5H_7O_2)_3 \cdot xH_2O$	-	crystalline powder	381403-50G 381403-250G
Dysprosium(III) acetate hydrate	$(CH_3CO_2)_3Dy \cdot xH_2O$	99.9	powder	325538-25G
Gadolinium(III) acetate hydrate	$Gd(CH_3CO_2)_3 \cdot xH_2O$	99.9	crystalline powder	325678-25G 325678-100G
Gadolinium(III) acetylacetonate hydrate	$Gd(C_5H_7O_2)_3 \cdot xH_2O$	99.9	powder	331716-5G 331716-25G
Neodymium(III) acetylacetonate hydrate	$Nd(C_5H_7O_2)_3 \cdot xH_2O$	-	-	460427-10G
Neodymium(III) isopropoxide	$Nd(OCH(CH_3)_2)_3$	99.8	-	410101-1G
Samarium(III) acetate hydrate	$(CH_3CO_2)_3Sm \cdot xH_2O$	99.9	powder	325872-25G 325872-100G
Samarium(III) acetylacetonate hydrate	$[CH_3COCH=C(O^-)CH_3]_3Sm \cdot xH_2O$	≥99.9	powder	517666-100G
Samarium(III) isopropoxide	$Sm[OCH(CH_3)_2]_3$	99.9	powder and chunks	410136-1G
Terbium(III) acetate hydrate	$Tb(CH_3CO_2)_3 \cdot xH_2O$	99.9	crystals and lumps	325929-5G 325929-25G
Terbium(III) acetylacetonate hydrate	$Tb(C_5H_7O_2)_3 \cdot xH_2O$	99.9	-	484008-1G
Terbium(III) tris(2,2,6,6-tetramethyl-3,5-heptanedionate)	$Tb(OCC(CH_3)_3CHCOC(CH_3)_3)_3$	98	-	434051-1G

For questions, product data, or new product suggestions, contact Aldrich Materials Science at matsci@sial.com.

ALDRICH® Materials Science

53

Rare-earth Vapor Deposition Precursors

For a complete list of available materials, visit aldrich.com/vapordeposition.

Name	Structure	Purity (%)	Prod. No.
Tris(tetramethylcyclopentadienyl)gadolinium(III)		99.9	511366-1G
Tris[N,N-Bis(trimethylsilyl)amide]gadolinium(III)		98	547824-1G
Tris(cyclopentadienyl)gadolinium(III)		99.9	492566-1G
Tris(cyclopentadienyl)terbium(III)		99.9	554006-5G
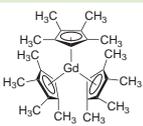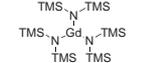
Magnetocaloric Materials

For a complete list of available materials, visit aldrich.com/magnetocaloric.

Name	Composition	Content (wt. %)	Form	Prod. No.
Dysprosium-Erbium-Aluminum alloy, $Dy_{0.8}Er_{0.2}Al_2$	$Dy_{0.8}Er_{0.2}Al_2$	Dysprosium 59.7 Erbium 15.6 aluminum 24.9	powder	693499-1G
Gadolinium-silicon-germanium alloy	$Gd_5Ge_2Si_2$	Gadolinium 79.5 Germanium 14.8 Silicon 5.7	powder and chunks	693510-1G
Gadolinium-silicon-germanium alloy	$Gd_5Ge_2Si_2$	Gadolinium 74.4 Germanium 24.2 Silicon 1.4	powder and chunks	693502-1G
Gadolinium	Gd	–	ingot	691771-10G

Ultra-high Purity Materials

Aldrich® Materials Science is pleased to offer a large selection of ultra-high purity metals, salts and oxides with purity of 99.999% or higher.

We offer over 300 metals, salts, and oxides with high trace metal purities and applications in areas including:

- Photovoltaics
- Magnetic Memory
- Phosphor Materials
- Biomedical Applications
- Nanoparticle Synthesis
- Electronic Devices

Name	Formula	Purity (Trace Metals Basis)	Aldrich Prod. No.
Europium(II) Bromide	$EuBr_2$	99.999%	751936
Zinc Chloride	$ZnCl_2$	99.999%	229997
Mercury	Hg	99.9999%	294594
Aluminum(III) Fluoride	AlF_3	99.999%	752983
Gallium(III) Chloride	$GaCl_3$	99.999%	427128
Zinc Fluoride	ZnF_2	99.999%	752819
Bismuth(III) Bromide	$BiBr_3$	99.999%	654981
Germanium(IV) Oxide	GeO_2	99.999%	483001
Germanium	Ge	99.999%	263230
Tellurium	Te	99.999%	204544
Lanthanum Oxide	La_2O_3	99.999%	203556
Barium Fluoride	BaF_2	99.999%	652458

Name	Formula	Purity (Trace Metals Basis)	Aldrich Prod. No.
Indium(I) Iodide	InI	99.999%	578606
Gold	Au	99.999%	326542
Aluminum Chloride	$AlCl_3$	99.999%	563919
Erbium(III) Bromide	$ErBr_3$	99.999%	575224
Holmium(III) Bromide	$HoBr_3$	99.999%	575232
Dysprosium(III) Bromide	$DyBr_3$	99.999%	575240
Silicon	Si	99.999%	267414
Copper	Cu	99.9995%	254177
Antimony(III) Oxide	Sb_2O_3	99.999%	202649
Cobalt(II) Chloride	$CoCl_2$	99.999%	409332
Lead(II) Iodide	PbI_2	99.999%	554359

For a complete list of ultra-high purity products, visit

aldrich.com/uhp

Working with Reactive, Volatile, Complex Materials to Produce Novel Alloys

Deborah L. Schlagel*, Andrew J. Sherve (not pictured), Thomas A. Lograsso
Division of Materials Science and Engineering
The Ames Laboratory, Ames, IA 50011
*Email: schlagel@iastate.edu

Introduction

Technologies are an integral part of our lives and we rely on them for such things as communication, heating and cooling, transportation, and construction. Improvements to technologies have made what they do for us more precise, automated, efficient, and powerful. One area of advancement is in the inclusion of components made from smart materials. Examples of this class of materials include actuators, transducers (a type of actuator), and sensors. Actuators take a signal and turn it into motion, and sensors convert physical changes into a signal. Performance metrics include sensitivity, responsiveness, resolution, and efficiency. Practical considerations include mass, volume, operating conditions, and durability. Smart materials possess some type of functionality that responds to the environment and can be exploited to do useful work. A smart alloy remembers its original cold-forged shape and will return to a pre-deformed shape when heated. Similarly, magnetostrictive alloys change their linear or volumetric shape when a magnetic field is applied which can be used to do mechanical work. When the magnetic field is removed, the material returns to its initial shape and size. Both smart and magnetostriction alloys are lightweight, solid-state alternatives to conventional actuators such as hydraulic, pneumatic and motor-based systems.

Another large area of research is in magnetocaloric materials where the material absorbs or gives off heat in a magnetic field. This type of heat pump has the potential to lower energy consumption by 20-30% over conventional vapor compression technology.[1] Particularly attractive are materials that have multiple functionalities that are interconnected because they are often more sensitive to input than their single-function counterparts. In general, the ideal material to fit a particular application needs to exhibit a controlled response to a stimulus that is reversible and repeatable indefinitely. In reality, functionality often diminishes over time due to fatigue or aging mechanisms, and much research is focused on increasing the efficiency and lifetime while keeping costs low. Finding a materials solution that satisfies many of these competing characteristics requires the discovery and design of novel materials.

Crystal Growth

The crystal growth method and conditions used depend on the chemical and thermodynamic properties of the alloy. Phase diagrams, and the literature they were developed from, are especially critical in assessing and identifying suitable crystal growth methods. When dealing with an alloy that contains volatile, reactive, corrosive, or high melting-point components, special attention is needed. In some cases, after an evaluation is made, it is determined that current methods or equipment are not up to the challenge either from a physical limitation or safety standpoint. In these cases, either modified or completely new protocols and capabilities are needed.

Single crystal characterization is ideal because it is in this form that the true nature and origins of the properties can be elucidated without the influences of extrinsic defects such as grain boundaries or second phases. Also, since single crystals can be cut along crystallographic directions, anisotropy of specific properties can be measured. Moreover, careful control of growth parameters can also minimize vacancies, defects and impurities at the microscopic level. These have direct bearing on the mesoscopic scale (i.e., magnetic domain wall movement) and on the macroscopic scale (i.e., bulk magnetic properties).

This paper will review crystal growth challenges of three different smart materials that have been a focus in Department of Energy's Ames Laboratory material synthesis and processing research initiatives. These materials (GdNi, Gd-Si-Ge, and Ni-Mn-Ga) are currently of interest to materials science research communities, and the capabilities developed to synthesize these materials with well-controlled stoichiometry and high structural quality have accelerated underlying understanding of their functionality. Our broader objective is to develop protocols applicable to other similar classes of materials to produce phase pure, single crystals of reactive and volatile metallic materials. For each of the above materials, we begin with a review of the initial single crystal growth attempts, discuss how specific challenges were addressed and conclude with some examples of characterization that were made possible by successful preparation of single crystal samples.

GdNi

The class of compounds formed between rare earths (RE) and 3d transition metals (TM) are of interest for their magnetic properties. Materials from this class of compounds benefit from the intrinsic properties of both components, i.e., from the high magnetic moment per atom, strong single-ion magnetocrystalline anisotropy and magnetostriction of the RE partner, and from the high magnetic coupling strength of the moments of the 3d TM partner.[2] The total number of these compounds is enormous since it is not uncommon for each RE-TM combination to give rise to multiple intermetallic compounds. Among them have been found outstanding permanent magnets ($RECo_5$), room temperature magnetostrictive alloys (RE-Fe, RE-Ni), and near atmospheric reversible hydrogen adsorption materials (i.e., $LaNi_5$) (Aldrich Prod. No. 685933).[2] In these investigations, to avoid crucible reaction with either the RE or TM, the polycrystalline materials were prepared either in an arc furnace or in a levitation furnace.

Here we look at the rare-earth intermetallic material, $Gd_{50}Ni_{50}$, which exhibits a magnetocaloric effect (MCE), making it a candidate for an alternative to conventional vapor compression refrigeration systems. It also exhibits spontaneous magnetostriction[3] at its Curie temperature on the order of 8,000 ppm,[4] which is remarkable considering the room temperature magnetostriction of iron (Aldrich Prod. No. 266256) and Terfenol-D are 45[5] and 2,000 ppm,[6] respectively. Single crystals for anisotropic property measurements were needed to fully understand the unusual coupling of its crystal structure to magnetism and the mechanism causing this compound's remarkably strong linear strain[4] along its c-axis. Because this is a congruently melting compound, the Bridgman method of crystal growth is a natural choice; however, it presents the challenge of identifying a crucible material. The particular combination of Gd (Aldrich Prod. No. 263060) and Ni (Aldrich Prod. No. 266965) ruled out common oxide crucibles, such as alumina (Aldrich Prod. No. Z247626), because of gadolinium's affinity for oxygen and also refractory metal crucibles, such as tungsten and tantalum, because of nickel's reactivity toward them. In fact, all readily available crucible materials were ruled out because of this alloy's very reactive nature.

Uhlirova et al.[7] prepared single crystal samples by the Czochralski method; however, no details were given concerning the growth. We first used a tri-arc crystal pulling technique,[8] which is a sister technique to that of Czochralski, where the charge sits on an actively cooled copper hearth (**Figure 1A**), which prevents it from fully melting and thus creates a self-crucible. However, sustained growth was not achieved because of arc instability at the low power used to maintain its relatively low melting temperature of 1,280 °C. The arcs were prone to wandering and becoming defocused which created hot and cold spots that favored recrystallization over continuous growth. Also, black body radiation overpowered the viewing lens making it difficult to visually observe the darker button (**Figure 1A**), which made dipping the seed and monitoring the crystal diameter during growth difficult. Increasing the mass of the button and the size of the tungsten stingers was attempted to increase the operating power needed and thus, improve arc stability. Unfortunately, these alterations, as well as varying growth parameters, only provided minimal improvements; and the resulting ingots were polycrystalline with grains too small to orient and cut for magnetization measurements.
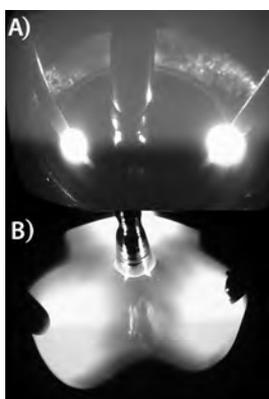
Figure 1. Tri-arc crystal pulling. The button is centered in a well in the copper hearth. A tungsten rod is the seed material and the three arcs are stationary during the run. **A)** GdNi: visibility is poor due to a lack of black body radiation at 1,280 °C. **B)** Gd-Si-Ge: in contrast at 1,850 °C, the seed/button interface and size of the overlapping pools are clearly visible.

Solution growth with a self-flux was also tried.[8] A Gd-rich starting composition of Gd_3Ni_2 was chosen, which has a lower melting point than GdNi and also a lower relative amount of nickel, making a pure tantalum crucible feasible. The Gd_3Ni_2 compound was melted and homogenized at 1,100 °C before slow cooling over a period of just over two weeks to a temperature above the 690 °C peritectic, where the remaining liquid was decanted off the crystals through a tantalum sieve inside of the crucible. Small plates resulted that grew along the a-axis in colonies. Analysis showed the crystals to be contaminated with trapped flux which produced its own magnetization signal and grains were too small for any measurements other than along the a-axis.

Single crystal growth by the Bridgman method is also reported in the literature. Nishimura et al.[9] used an alumina crucible but Sato[10] did not provide any details. Neither provided characterization beyond magnetic measurements; however, optical and scanning electron microscopy (SEM) with energy-dispersive spectroscopy (EDS) of our crystal growth[8] attempt in Al_2O_3 revealed multiple secondary phases visible at low magnification that incorporated both the aluminum and oxygen from the crucible. Yttria was also tried as it is a thermodynamically more stable oxide than Gd_2O_3 and should have been inert with respect to Gd.

However, we found the reaction zone to be quite extensive, with yttria dissolving and reacting with the alloy as well as gadolinium substituting for the yttrium in the oxide. Tantalum Bridgman crucibles with a tantalum boride or tantalum carbide coating that were produced in-house by a procedure developed by Gschneidner, Jr. et al.[11] were also tried. The carbide coating was not as successful as the boron coating, and from our analysis[8] we found that further processing was necessary to remove the active boron from the surface before use. We took crucibles made by their method and melted a relatively inexpensive pure rare earth in it, such as yttrium. The yttrium reacted with the surface boron and presumably converted TaB to the more thermodynamically stable Ta_2B. The yttrium was then etched out of the crucible before use. The crystal growth resulted in single crystal grains suitable for magnetization and resistivity anisotropic measurements. In parallel with this crucible development, we also prepared yttria stabilized zirconia (YSZ) and gadolinia plasma sprayed Bridgman crucibles.[8] The crucibles were backed with tungsten for strength. We did not find the YSZ to be an improvement over the yttria crucibles mentioned above; however, the Gd_2O_3 crucible yielded a remarkably clean ingot with few grains. The large, single phase grains enabled a full suite of magnetization, resistivity, and heat capacity measurements to be done.

Figure 2 shows select isothermal magnetization versus field curves from samples made by three different groups along the *b*-axis for single crystals. The inverse relationship between magnetization and temperature is maintained in fields above 30 kOe, regardless of growth specifics. Below 30 kOe, there was some minor variation in curve shape that caused some of the scans to cross. The calculated maximum entropy change, $-\Delta S_M^{max}$, for this crystal[8] in differential fields of 20 and 50 kOe is slightly higher at 9.82 and 19.2 J/kg K compared to 9 and 17 J/kg K measured on polycrystalline GdNi.[12] These comparisons indicate that the magnetic properties of GdNi may not be sensitive to impurities, processing routes, or even long range atomic order. Paudyal et al.[4] utilized first principles spin polarized calculations to explain the isotropic behavior seen in single crystals as a function of magnetic field and temperature as arising from the unusual interplay between magnetism and crystal structure.
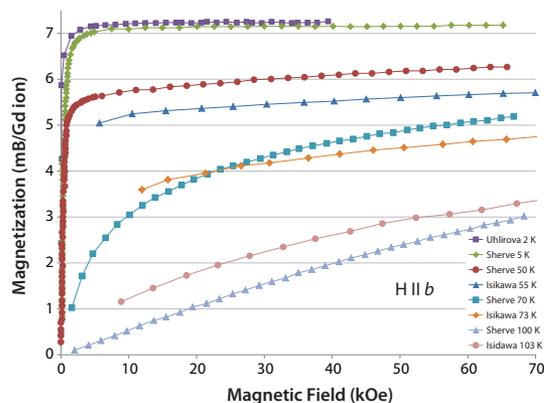
Figure 2. Isothermal magnetization curves for single crystal GdNi along the b-axis. The data from three different samples follow the trend of increasing magnetization with temperature.

For questions, product data, or new product suggestions, contact Aldrich Materials Science at **matsci@sial.com**.

57

GdSiGe

The family of compounds $RE_5(Si_xGe_{1-x})_4$ has become known for its giant MCE near room temperature. They were also discovered to have unusually large magnetostriction and magnetoresistance, which makes them viable actuators, transducers, and sensors candidates. In this alloy, both Gd and Si raise crucible compatibility concerns. Quartz or silica is normally used for Si, but Gd reacts with oxygen in these materials and they cannot withstand the high melting temperatures of these alloys. Silicon easily wets many crucible materials, requiring a closed crucible system to prevent silicon loss. Tungsten, a weldable refractory crucible material, is resistant to rare earth metal attack and not prone to silicide formation, making it a good candidate.

The first successful growth of large crystals of $Gd_5Si_2Ge_2$ (Aldrich Prod. No. 693510) suitable for anisotropic materials property investigations was done in a tungsten crucible by the Bridgman method.[13] Tungsten crucibles were indeed found to be inert, i.e., no formation of tungsten silicide or germanides. There was a slight solubility of tungsten in the molten alloy which resulted in precipitation of pure tungsten dendrites in the bulk alloy and along the crucible walls. The latter led to strong mechanical bonding between the crucible and ingot. Upon cooling, the ingot developed cracks due to thermal expansion mismatch between $Gd_5Si_2Ge_2$ and tungsten. Also, the properties varied along the length proportional to the chemical segregation which followed the relation:

$$C = kC_o(1-g)^{k-1} \tag{1}$$

for solute redistribution during solidification of an alloy where C is concentration in the solid at position along the growth, where a fraction g of the original liquid has frozen, C_o is the nominal composition, and k is distribution coefficient. While anisotropic single crystal measurements were possible with samples harvested from these Bridgman crystal growths, there was still a need to have tungsten and crack-free samples to ensure these features were not adding to or detracting from the true properties of the material. It was also desirable to produce chemically homogeneous ingots with uniform properties. Significant improvement was achieved by utilizing the tri-arc crystal pulling method.[14] As described in the previous section, this is a crucible-less method so the problems with crucible contamination and cracks resulting from thermal mismatch were avoided. Also, with no crucible for the Si to wet, it stayed in solution which helped minimize composition variation along the length of the growth.

With the tri-arc crystal pulling method, the ingot size is limited to several millimeters in diameter because of the latent heat of the stingers. To try and keep this heat from melting the surface of the growing crystal, we increased the stinger to crystal distance and reduced the stinger size to better focus the heat. We quickly found, there is limited latitude for both of these variables and even minor changes result in disruption of the delicate heat flow balance at the growth interface and growth cannot be sustained. The length of the growth is also limited to less than 5cm by the button volume/size which is directly proportional to both the crystal-stinger distance and the heat needed for the molten pools to effectively overlap (Figure 1B). Nonetheless, the resulting ingots were of sufficient quality and size for numerous characterization studies. Figure 3 shows the magnetization dependence on crystallographic direction with varying field and temperature for $Gd_5Si_2Ge_2$. Systematic characterization of the family of $R_5(Si_xGe_{1-x})_4$ compounds, utilizing both bulk and single crystal samples, led to the discovery of the extreme sensitivity of the crystal and magnetic lattices to the chemical composition, temperature, magnetic field, and pressure[15] of many of the members. Also, single crystals have allowed the detailed study of the atypical Widmanstätten features[16] found in all alloys of this family, elucidation of its elastic properties[17] and response to hydrostatic pressure.[18]
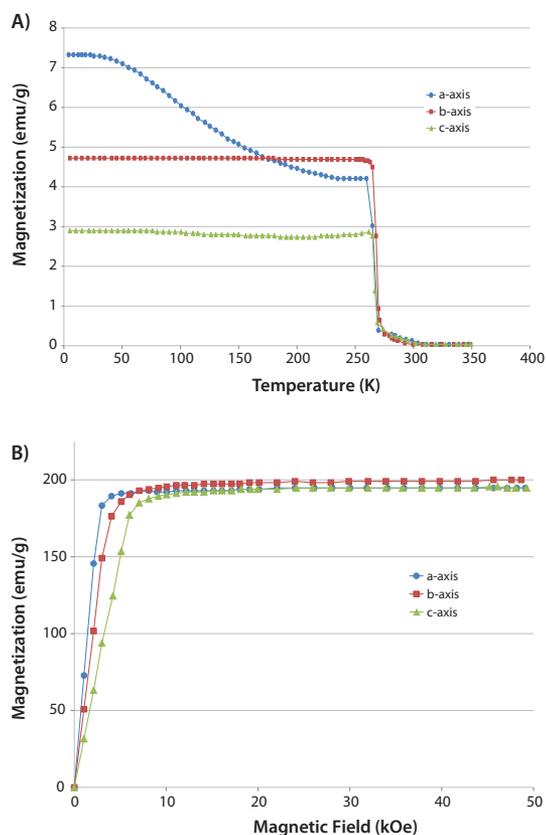
Figure 3. Magnetic characterization of $Gd_5Si_2Ge_2$ single crystal along the three crystallographic axes. **A)** Magnetization as a function of temperature in a magnetic field of H=100 Oe. **B)** Field dependence of magnetization at T=5 K.[18]

NiMnGa

Field-induced actuators can overcome the disadvantage of traditional thermal, pneumatic, hydraulic, and motor-based shape-memory actuators as they exhibit a fast frequency shape-memory effect in a magnetic field. The lead contenders are intermetallic alloys that adopt the face-centered cubic Heusler structure. These alloys typically undergo a crystallographic disorder-order transition at high temperature and the ordered structure undergoes a reversible martensitic shear transformation at room temperature or below. When the martensite transformation is near the Curie temperature, or coupled to magnetic ordering, applied magnetic fields can drive the structural rearrangements between the low symmetry martensitic phase and the high symmetry austenitic phase. These rearrangements, facilitated by twin boundary motion, result in reversible shape changes. Ferromagnetic Ni-Mn-Ga displays the largest shape changes of all known magnetic Heusler alloys with magnetic field induced strains reaching 10%.[19] Also, its magnetic properties are highly composition-dependent, potentially making its response tunable for particular applications. The strain was determined to be crystallographically anisotropic and the martensitic phase to consist of numerous structural variations, many of which differ only in the stacking sequence of their atomic layers. Which variations are present depends on composition and thermal history. Also, the sequence of martensitic, premartensitic and intermartensitic transformations are important to its performance as a shape-memory alloy. When this behavior is present, it is manifested as bumps in differential scanning calorimetry (DSC). One example of this is shown in **Figure 4**. Even though the bumps appear to be erratic, they are reproduced each time the sample is cycled.
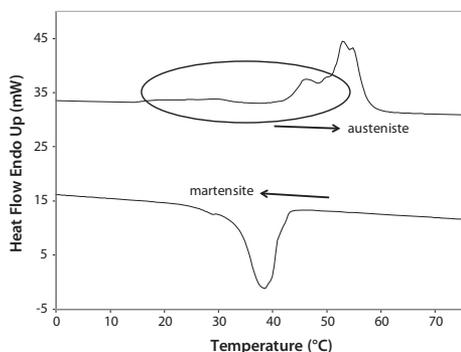
Figure 4. Differential Scanning Calorimetry (DSC) of $Ni_{49}Mn_{30}Ga_{21}$, 20 °C/min. Features in oval indicate possible premartensitic or intermartensitic transitions and are repeated with cycling.

Alloy preparation of this material is fairly straight forward as the Heusler structure is a solid solution that exists over a large compositional field, but volatility of Mn can be an issue. While a wide phase field is beneficial to alloy preparation, it negatively impacts the ability to grow chemically homogeneous single crystalline ingots due to chemical segregation from non-congruent melting behavior. Samples with uniform and predictable magneto-mechanical responses for scientific research, and ultimately for device applications, require tight control of the growth process especially since the properties and functionality of these alloys are highly composition dependent.

Initial attempts to prepare stoichiometric Ni_2MnGa or off-stoichiometric alloys resulted in several grains elongated along the length of the ingot. This initiated a study[20] to determine the primary solidification phase field of Ni_2MnGa. With this knowledge of the phase equilibria, experiments were conducted to find the proper growth parameters for the Czochralski and Bridgman techniques to produce larger grains, if not single grain ingots. Some success was made with the Czochralski method but consistently large single crystals (1.5 cm diameter × 6 cm long) were first obtained by the Bridgman method from Ni-deficient compositions using a growth rate of 2.0 mm/hr. Although manganese and gallium evaporative losses were easily mitigated by over-pressurization during growth, significant macrosegregation of composition varied along the length of the ingot (**Figure 5**); and according to **Equation 1**, resulted in significant differences in properties from one end to the other, even with post-growth annealing.
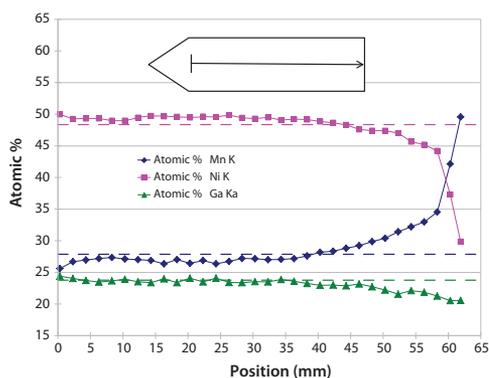
Figure 5. Electron dispersive spectroscopy (EDS) chemical analysis along the growth direction. The horizontal lines show the nominal composition of the ingot; 5 mm/hr growth rate. Chemical segregation of the elements follow **Equation 1**.

From here, further improvements to the crystal growth processing were quickly realized to reduce compositional segregation and produce uniform material. Sozinov et al.[21] prepared crystals at 30 mm/hr and of sufficient size to make uniform, oriented samples 5×5×10 mm^3. Liu et al.[22] was successful in obtaining single crystals up to 6-10 mm diameter × 20-80 mm long by the Czochralski method using a cold crucible system with growth rates ranging from 5-30 mm/hr and make oriented samples 2×9×12 mm^3. Chu et al.[23] grew a crystal by the Bridgman method but their starting materials were in the form of powders, which resulted in multiple grains and minor second phases evidenced by the presence of microstructure. This emphasizes the importance of chemical purity of the starting materials since impurities can be sources of grain nucleation and can impede the magneto-mechanical response of the material. No mention of chemical variation along the length was made by either Sozinov or Liu; however, Jiang et al.[24] undertook a comprehensive study of parameters such as temperature gradient, zone length, crystal growth velocity and diameter on the growth interface morphology, preferential crystallographic growth direction, and resulting chemical variation along the length. Through the use of optical zone-melting directional solidification, Jiang was able to obtain preferentially <100> oriented ingots 7×100 mm with much less property variation along the length than with the Bridgman method. Later, this group[25] used this method to grow single crystals for the purpose of studying the solute partitioning during crystal growth to further eliminate compositional variation along the length. They looked at three compositions (stoichiometric, Ni-rich, and Mn-rich) and were able to produce rods with no obvious macro segregation after the initial 20 mm at a growth rate of 5 mm/hr. A patent was issued in 2009 for the electroslag remelting Bridgman process.[26] The advantage of this method is the slag encapsulates the melt so there is no crucible interaction and the feed material is purified by crystalizing out of the slag, which also decreases the number of pores and occlusions. The result is a production-scale crystal essentially free of the defects that are thought to impede the twin boundary or domain wall motion responsible for its large magnetostriction. Sturz et al.[27] were also interested in production-scale crystal growth. They designed a crucible that simultaneously grows four to six crystals that are 20-30 mm in diameter × 110 mm long. Starting from polycrystalline as cast material, through the use of a grain selector and post-growth annealing, they were able to produce single crystals with longitudinal axes that were within 10 degrees of the [100] direction and the composition only varied ±0.6% from end to end. In 2011, Brillo et al.[28] reported computer simulation results predicting the thermal profile of their Bridgman-Stockbarger furnace for Ni-Mn-Ga single crystal growth. The benchmark parameters established can be utilized to predict optimum growth conditions in a particular system if the thermal properties and heat transfer coefficients of its components are known.

While the mechanisms that lead to Ni-Mn-Ga large field induced strain are still not well understood and research continues, this particular alloy has completed the cycle of crystal growth development to production development and deployment of commercially available actuators and devices.

For questions, product data, or new product suggestions, contact Aldrich Materials Science at **matsci@sial.com**.

ALDRICH Materials Science

59

Conclusions

As the desire for even smaller, smarter, more efficient, and longer life devices continues, research is starting to revisit previously overlooked candidate materials that were thought to be too corrosive, reactive, or their properties too irreproducible. While the end goal may be commercial production, in the research stage of a material's development single crystals are fundamental in characterizing its properties and full capabilities unmodified by grain boundaries or impurities. The barriers to the crystal growth of three alloys containing reactive or volatile components as well as displaying varied physical properties as a result of chemical segregation, has been addressed.

Acknowledgment

References

(1) Gschneidner, K.; Pecharsky, V., *International Journal of Refrigeration-Revue Internationale Du Froid*, **2008**, 31, 945.
(2) Buschow, K.H.J., *Reports on Progress in Physics*, **1977**, 40, 1179.
(3) Gratz, E.; Lindbaum, A., *Journal of Magnetism and Magnetic Materials*, **1998**, 177, 1077.
(4) Paudyal, D.; Mudryk, Y.; Lee, Y. B.; Pecharsky, V.K.; Gschneidner, K.A.; Harmon, B.N., *Phys. Rev. B,* **2008**, 78, 184436.
(5) Xing, Q.; Lograsso, T.A.; Ruffoni, M.P.; Azimonte, C.; Pascarelli, S.; Miller, D.J., *Appl. Phys. Lett.*, **2010**, 97, 072508.
(6) Clark, A. *Ferromagnetic Materials*: North-Holland, Amsterdam, 1980.
(7) Uhlírová, K.; Prokleška, J.; Poltierová Vejpravová, J.; Sechovský, V.; Maezawa, K., *J. Mag. Mag. Mat.*, **2007**, 310, 1753.
(8) Sherve, A., Iowa State University, 2011.
(9) Nishimura, K.; Mori, K.; Narita, Y.; Hutchison, W. D., *J. Mag. Mag. Mat.*, **2007**, 310, 1730.
(10) Sato, K., *Transactions of the Japan Institute of Metals*, **1980**, 21, 336.
(11) Gschneidner, K.A.; Schmidt, F.A., "Determination of the Optimum Processing Parameters for the Preparation of Carbide Coated Refractory Metal Objects.," the Ames Laboratory, 2008.
(12) Kumar, P.; Suresh, K.; Nigam, A.; Gutfleisch, O., *Journal of Physics D-Applied Physics*, **2008**, 41.
(13) Lograsso, T.A.; Schlagel, D.L.; Pecharsky, A.O., *Journal of Alloys and Compounds* **2005**, 393, 141.
(14) Schlagel, D.L.; Lograsso, T.A.; Pecharsky, A.O.; Sampaio, J.A., Technical Session of Light Metals, 2005, held at the 134th TMS Annual Meeting, San Francisco, California, 2005; p. 1177.
(15) Pecharsky, V.; Samolyuk, G.; Antropov, V.; Pecharsky, A.; Gschneidner, K., *Journal of Solid State Chemistry*, **2003**, 171, 57.
(16) Ugurlu, O.; Chumbley, L.S.; Schlagel, D.L.; Lograsso, T.A., *Acta Materialia*, **2006**, 54, 1211.
(17) Svitelskiy, O.; Suslov, A.; Schlagel, D.L.; Lograsso, T.A.; Gschneidner, K.A.; Pecharsky, V. K., *Phys. Rev. B*, **2006**, 74.
(18) Magen, C.; Morellon, L.; Algarabel, P.; Ibarra, M.; Arnold, Z.; Kamarad, J.; Lograsso, T.; Schlagel, D.; Pecharsky, V.; Tsokol, A.; Gschneidner, K., *Phys. Rev. B*., **2005**, 72.
(19) Pagounis, E., *Mat. Sci. Eng. Rev.*, **2007**, 56, 33.
(20) Lograsso, T.A.; Schlagel, D.L.; Zhang, W.; Wu, Y.L., "Crystal Preparation of Ni-Mn-Ga Alloys: Final Report," Institute for Physical Research and Technology: Iowa State University, 1999. *See also* Schlagel, D.L.; Wu, Y.L.; Zhang, W.; Lograsso, T.A., *Journal of Alloys and Compounds*, **2000**, 312, 77.
(21) Sozinov, A.; Likhachev, A.A.; Ullakko, K., *SPIE*, **2001**, 189.
(22) Liu, G.; Chen, J.; Cui, Y.; Liu, Z.; Zhang, M.; Wu, G.; Brück, E.; de Boer, F. R.; Meng, F.; Li, Y.; Qu, J., *Solid State Communications*, **2004**, 130, 687.
(23) Chu, S.Y.; Gallagher, R.; De Graef, M.; McHenry, M.E., *IEEE Trans. Magn.*, **2001**, 37, 2666.
(24) Jiang, C.; Liu, J.; Wang, J.; Xu, L.; Xu, H., *Acta Materialia*, **2005**, 53, 1111.
(25) Wang, J.; Jiang, C., *J. Crys. Growth*, **2008**, 310, 865.
(26) Fiechter, S.; Mecklenburg, A.; Nabien, H.-P.; Schneidner, R.P.; C30B 11/00C22B 9/16B22D 27/04C30B 29/10C30B 9/00C22B 9/18C30B 29/02B22D 1/00C30B 29/52C22B 23/00C22B 23/06 ed.; Hahn-Meitner-Institut Berlin GmbH: Germany, 2009.
(27) Sturz, L.; Drevermann, A.; Hecht, U.; Pagounis, E.; Laufenberg, M., *Physics Procedia*, **2010**, 10, 81.
(28) Brillo, J.; Behnken, H.; Drevermann, A.; Plevachuk, Y.; Pagounis, E.; Sklyarchuk, V.; Sturz, L., *International Journal of Heat and Mass Transfer*, **2011**, 54, 4167.

Materials for Crystal Growth

For a complete list of available materials, visit aldrich.com/periodic.

Gadolinium and Nickel

Name	Composition	Purity (%)	Form	Prod. No.
Gadolinium	Gd	99.9	chips	263087-10G 263087-50G
Gadolinium	Gd	99.9 (REM)	foil	693723-1EA
Gadolinium	Gd	99.99 (REM)	ingot	691771-10G
Gadolinium	Gd	99.9	ingot	261114-10G
Gadolinium	Gd	99	powder	263060-5G
Nickel	Ni	99.98	foil	357553-2.8G 357553-11.2G 357553-44.8G
Nickel	Ni	99.995	foil	267007-1.4G 267007-5.6G
Nickel	Ni	99.98	foil	357588-2.2G 357588-8.8G
Nickel	Ni	99.999	powder	266965-50G
Nickel	Ni	99.99	powder	203904-25G 203904-100G 203904-500G
Nickel	Ni	99.7	powder	266981-100G 266981-500G
Nickel	Ni	99.8	powder	268283-25G
Nickel	Ni	≥99.99	rod	267074-14G 267074-42G
Nickel	Ni	≥99.99	wire	267058-1.7G 267058-8.5G

Germanium and Silicon

Name	Composition	Purity (%)	Form	Prod. No.
Germanium	Ge	99.999	chips	263230-10G 263230-50G
Germanium	Ge	99.999	chips	203343-5G 203343-25G
Germanium	Ge	≥99.999	powder	327395-5G 327395-25G
Germanium	Ge	≥99.99	powder	203351-10G 203351-50G
Silicon	Si	99.95	pieces	343250-50G 343250-500G
Silicon	Si	99.999	powder	267414-25G
Silicon	Si	99	powder	215619-50G 215619-250G 215619-1KG

Manganese and Gallium

Name	Composition	Purity (%)	Form	Prod. No.
Manganese	Mn	99	chips	266167-500G
Manganese	Mn	≥99	powder	266132-250G 266132-1KG
Manganese	Mn	99.99	powder	463728-25G 463728-100G
Gallium	Ga	99.9995	-	203319-1G 203319-5G 203319-25G
Gallium	Ga	99.999	-	263273-10G 263273-50G
Gallium	Ga	99.99	-	263265-10G 263265-50G

For questions, product data, or new product suggestions, contact Aldrich Materials Science at **matsci@sial.com**.

ALDRICH®
Materials Science

61

Vistas in Current Magnetic Materials Research

K. G. Suresh
Department of Physics
IIT Bombay
Mumbai, India
Email: suresh@phy.iitb.ac.in

Introduction

Magnetism and magnetic materials have been of scientific interest for over 1,000 years. More recently, fundamental investigations have focused on exploring the various types of magnetic materials and understanding magnetic effects created by electric currents. The practical exploitation of the latter has resulted in a large number of devices which are indispensable today. The development of the field of magnetism in materials started as a curiosity to understand this new and exciting phenomenon, but soon it materialized as an enormous reservoir for many practical or applied materials. In this context, the "miracle" material was magnetite (Fe_3O_4) (Aldrich Prod. No. 310069), which is also known as ferrites. Ferrites represent a large class of magnetic materials with high potential in a diverse range of applications. In a way, the history of magnetic materials research is synonymous with the development of ferrites, both for fundamental studies as well as for their potential commercial applications. As with other magnetic materials, ferrites may be classified as both soft and hard materials and find extensive applications ranging from microwave devices to permanent magnets.[1]

Along with ferrites, ceramic and metallic materials in bulk, thin film, and nano forms constitute the backbone of magnetic materials research in industry today. Amorphous magnetic materials also offer great interest and potential by virtue of their peculiar magnetic properties. In addition, magnetism of molecular materials is very attractive because of the exciting properties of many such molecules. The projected applications of magnetic materials range from biomedical fields to quantum computing.

From the point of view of condensed matter physics or materials science, apart from ferrites, another major class of materials is intermetallic compounds containing rare-earth and/or transition metals.[2] The magnetic behavior of these materials is due to transition metal (T) ions, rare-earth (R) ions, or a combination of the two. These alloys, in general, have the advantage that they are mostly ferromagnetic with large saturation magnetization, Curie temperature, and magnetic anisotropy. In fact, these alloys constitute the bulk of permanent magnets used in devices today. Moreover, these R-T compounds have tunable magnetic properties, which are advantageous for many applications, as discussed in later sections of this article. Many interesting properties also arise when rare earths or transition metals are alloyed with nonmagnetic elements such as Si, Ge, Sb, etc. Some of the best-in-class materials discovered in the immediate past belong to this class. However, due to the exorbitant cost of rare earths, systems based on transition metals are becoming increasingly popular.

Many practical applications of magnetic materials arise from the coupling of magnetism and other physical properties. These include magneto-transport, magneto-thermal, magneto-elastic, magneto-optic, magneto-electrical, and magneto-structural couplings. These properties give rise to phenomena such as magnetoresistance, the magnetocaloric effect, magnetostriction, shape-memory effects, and magneto-impedence, to name a few. Some of these properties and the way they are commercially exploited are presented in this article.

Magnetic Recording and Spintronics

Historically, apart from permanent magnets, the major application of magnetic materials has been in magnetic recording, a field that has been revolutionized every decade with new breakthroughs in magnetic materials research.[3,4] Magnetic recording is one of the most widespread applications of magnetic materials today. It was reported that the annual data storage capacity in the world reached 5×10^{10} GB in 2002, or about 800 MB per year per person. Among the various forms of data storage, hard disc drives (HDD) are the largest contributor. Recording media can be classified as longitudinal or perpendicular, depending on the orientation of the magnetic domains. Perpendicular media can provide much larger recording densities than longitudinal media. In the 1980s, Co-Cr based alloys were regarded as the only feasible alloy system for media of HDDs. However, in the 1990s, it was extended to include Co-Cr-Pt and Co-Cr-Ta alloys. By the 2000s, Co-Cr-Z (Z=Pt, Ta, B, etc.) for longitudinal recording media and Co-Cr-Pt-SiO$_2$ metal oxide granular films for perpendicular recording media were also included. The two-phase microstructure, as well as the large magnetocrystalline anisotropy of the Co-Cr system, offers many advantages in the HDD design. Other potential systems pursued for high density recording are Co-Mo(W), FePt, CoPt, and rare-earth based compounds such as SmCo$_5$ (Aldrich Prod. No. 339229) and NdFeB (Aldrich Prod. No. 693790). The latter two compounds have previously attracted little notice, possibly because of their much larger magnetic anisotropy as well as their poor ability to crystallize during sputtering processes. In order to achieve recording densities greater than 1 Tb/in^2, techniques such as percolation perpendicular media and bit patterned media were actively investigated.[5-8]

For magnetic recording applications, materials in particulate, thin film, or multi-layer form are usually used. The ground-breaking discovery of spintronics has added a new dimension to the field of magnetic recording.[9-12] Stored magnetic information from the disk is read with the help of giant magnetoresistance (GMR). The discovery of GMR in a magnetic multilayer system (Fe/Cr/Fe) in 1988 was a breakthrough in the history of modern magnetic materials research, both from fundamental physics as well as application perspective, and was awarded the Nobel prize in 2007. In conventional electronics, one controls the charge of the electron and its manipulations with the help of an electric field. But in spintronics there is an additional degree of freedom, namely the spin of the electron, which can be controlled by a magnetic field. Half-metallic ferromagnets and spin-polarized transport are key concepts associated with the physics of spintronics. The field of spintronics continues to grow and is supplemented with the new developments in magnetic thin films and nanomaterials research. The first commercial application of spintronics in sensors for the automotive industry appeared in 1993. This was followed by the commercialization of GMR heads (**Figure 1**) in magnetic memory in 1997, which led rapidly to an increase of the density of information stored on disks (from 1 Gb/in^2 to 600 Gb/in^2) by the end of 2007. Today, spintronics encompasses many promising new phenomena such as spin transfer, magnetic semiconductors, molecular spintronics, organic spintronics, and single-electron spintronics. A key phenomenon associated with spintronics is the tunnel magneto-resistance (TMR) exhibited by magnetic tunnel junctions (MTJs). MTJs are the basis of a new concept of magnetic memory called Magnetic Random Access Memory (MRAM), which combines short access time of

semiconductor-based RAMs and the non-volatile character of magnetic memories.[13] The first commercial MRAM entered the market in 2006. The next generation of MRAM, using a switching process by spin transfer, is expected to have a big impact on computer technology.

Monopole Inductive Write Head
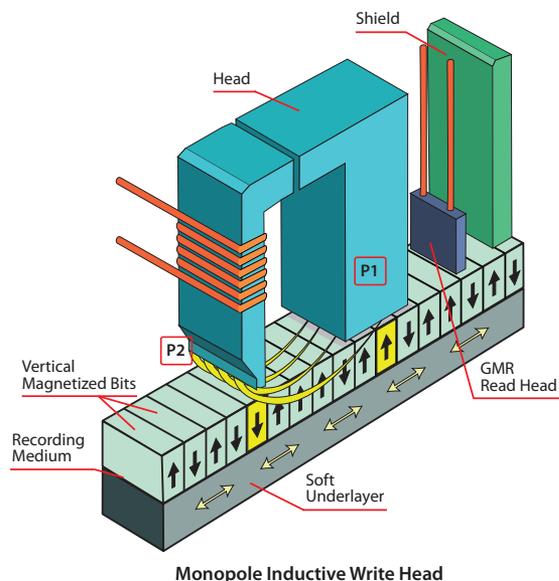
Figure 1. Diagram showing the magnetic read-write in a perpendicular recording medium. Adapted from Reference 33.

Magnetic semiconductors constitute an important field today because of the possibilities of good spintronic materials and devices.[14] Magnetic semiconductors are very attractive because of their ability to combine potentials of conventional semiconductors (namely, control of current by gate, coupling with optics, etc.) with those of magnetic materials (control of current by spin manipulation, nonvolatility, etc.). One of the outcomes of this integration is the Spin Field Effect Transistors (Spin FETs) based on spin transport in semiconductor lateral channels between spin-polarized source and drain with control of spin transmission by a field effect gate. Research on magnetic semiconductors is mainly concentrating on 1) hybrid structures combining ferromagnetic metals with nonmagnetic semiconductors; 2) ferromagnetic semiconductors belonging to the $Ga_{1-x}Mn_xAs$ family; and 3) the Spin Hall effect, which can create spin currents in structures composed solely of nonmagnetic conductors. Other systems being pursued with interest in spintronics include ZnXO (x=Ni, Mn, Co) and GaMnN. Search for potential spintronics materials is also concentrating on the half-Heusler family of alloys. The prototypical alloy of this series is NiMnSb, which has been found to be a good half metallic ferromagnet.

Spintronics has emerged as one of the most fascinating topics in magnetic materials research today. Its potential applications, though conceived over a wide range, are yet to be fully exploited. For example, the quantum mechanical nature of the spin and the long spin coherence time in confined geometries offer great potential in the field of quantum computing. There is no doubt that spintronics will take an important place in the technology of our century.

Exchange Bias and Magnetostrictive Materials and Applications

A topic closely related to magnetic recording is the phenomenon of exchange bias. Exchange bias results in a shift of the hysteresis loop with respect to the magnetization axis, thereby providing a DC field bias.[15] Such a phenomenon is attributed to exchange anisotropy, usually associated with ferromagnetic-antiferromagnetic interfaces. Unlike the uniaxial anisotropy seen in bulk magnetic materials, exchange bias is a result of unidirectional magnetic anisotropy. A family of alloys known as magnetic shape-memory alloys is found to show large exchange bias (**Figure 2**). Exchange bias has become quite important from the technological point of view because it can be used to fix the magnetization of a ferromagnetic layer, which serves as the reference layer, in a magnetic sensor. Because of the strong application potential, there is a huge demand for systems that show large exchange bias at room temperature and above.
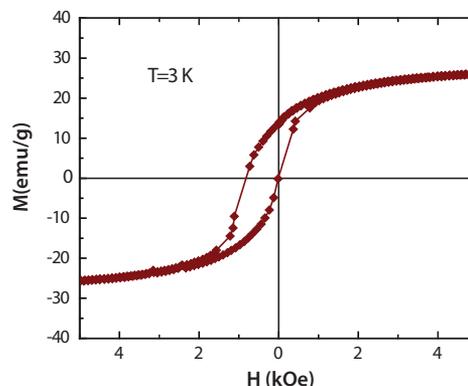
Figure 2. Exchange bias in a full Huesler alloy.

Magnetic sensors, transducers, and actuators constitute another important area of application of magnetic materials. The main underlying property that enables this application is magnetostriction,[16] which is the most important magneto-elastic phenomenon exhibited by magnetic materials. This is a phenomenon where the dimensions of a magnetic material change when an external magnetic field is applied. By applying a time varying magnetic field, one can set a magnetic rod into vibration, thereby convert the electrical/magnetic energy to mechanical energy. This principle can be used for energy conversion or sensing. So-called magnetostrictive transducers are being used extensively in sonar. Magnetostrictive transducers have many advantages over piezoelectricity-driven devices such as the PZT (Lead Zirconate Titanate) devices. Rare-earth transition-metal intermetallic $(Tb,Dy)Fe_2$ (commercially known as Terfenol-D) is a high efficiency solid-state transducer and was one of the most attractive magnetostrictive material in the 1980s and 1990s. The magnetostriction of this material generates strains 100 times greater than traditional magnetostrictive materials, and about five times greater than traditional piezo-ceramics. Terfenol also has a high Curie temperature, making it suitable for room-temperature applications. Furthermore, by adjusting the stoichiometry of the alloy, this temperature range can be extended down to cryogenic temperatures. However, large magnetocrystalline anisotropy of many such R- intermetallic compounds limits application, in spite of their giant magnetostrictive properties. Recently, $Fe_{1-x}Ga_x$ alloys have emerged as potential successors to R-T compounds because of their large magnetostriction and good mechanical properties at low fields.[17] Additionally, chemical and structural heterogeneity and the resulting interaction of coexisting phases in textured $Co_{1-x}Fe_x$ thin films is reported to result in large magnetostriction at very low fields. Microstructural analysis of this result

For questions, product data, or new product suggestions, contact Aldrich Materials Science at **matsci@sial.com**.

ALDRICH
Materials Science

63

has revealed the giant magnetostriction is associated with the precipitation of an equilibrium Co-rich fcc phase embedded in a Fe-rich bcc matrix. This result indicates a route to the discovery of giant, low-field magneto-elastic materials.

Research in the field of magneto-elastic phenomena has resulted in a new class of materials known as ferromagnetic shape-memory alloys.[18] The most striking example of this family is a set of compounds known as full Heusler alloys with the composition X_2YZ (X and Y are transition metals, and Z is a nonmagnetic element). The magnetic field induced strain in many of these alloys is quite large compared to that of conventional magnetostrictive materials. One of the first materials to show this effect was Ni_2MnGa. Subsequent to this discovery, a large number of stoichiometric and non-stoichiometric alloys of the 2:1:1 family with different elements have been tested. This has resulted in the identification of several potential ferromagnetic shape-memory alloys, in bulk and thin film form.[19] These materials are usually multifunctional, with significant changes in properties such as electrical resistance and magnetic entropy as a function of the applied magnetic field. From the point of view of fundamental magnetism, shape memory materials in general, and full Heusler alloys in particular, are very important because they show a first order coupled magneto-structural transition. The strong magneto-structural coupling is responsible for many anomalous properties of this series.

Magnetic Refrigeration

Magnetic cooling is a relatively new application of magnetic materials.[20] Magnetic cooling is based on the principle of adiabatic demagnetization of a magnetic material wherein magnetic entropy of the solid is manipulated by changing the applied field. This gives rise to desired changes in temperature, thereby enabling cooling (refrigeration) or heating (heat pumps) applications. The main advantages of magnetic refrigerators are based on their eco-friendly nature and anticipated superior performance compared to existing conventional gas-based refrigerators. The efficiency, compactness, and adaptability of magnetic refrigerators have given the field of magnetic cooling a separate and recognized identity. In view of these advantages, magnetic refrigeration is termed as "green and clean" technology.

Though chronologically speaking, magnetic cooling/heating is not a new idea, exploitation of ferromagnetic materials for this application has revolutionized the concept in a significant manner. The central component of a magnetic refrigerator (**Figure 3**) is a magnetic material which possesses a very high (giant) magnetocaloric effect (MCE). An MCE manifests as isothermal magnetic entropy change or adiabatic temperature change when the material is subjected to a magnetic field. The other components are the field generating magnet assembly and the design that result in cooling of the desired volume. The higher the MCE, the smaller the field required; thus, the practical design of a working refrigerator demands materials with giant MCE. From the commercial point of view, it is desirable that the refrigerator works in fields that can be generated by permanent magnets. Therefore, giant magnetocaloric materials are of great importance. The terminology of giant magnetocaloric effect (GMCE) came into existence with the ground-breaking discovery of large MCE in $Gd_5Ge_2Si_2$ (Aldrich Prod. No. 693510) by Pecharsky and Gschneidner.[21] Since then, various materials systems have been studied to identify such materials. Usually, materials that undergo first-order magnetic transitions/magneto-struc-tural transitions possess GMCE,[22] and most current work tries to address this issue. Many systems in this family have been developed in the recent past, mainly from the rare-earth intermetallics family. As all potential permanent magnets are also made of rare earths, the

development of low field (efficient, viable) magnetic refrigeration technology implies a huge demand/market for rare earths. In fact, this has led to vigorous exploration and extraction/recovery of various rare earths throughout the world.
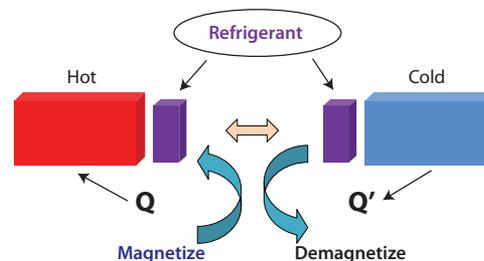
Figure 3. Schematic of vital components of a magnetic refrigerator.[24]

While GMCE materials are highly important, there are several challenges associated with them. Main challenges are the large thermal hysteresis associated with the first order transition and the long delay in achieving the maximum adiabatic temperature change. Another problem is to get the refrigerants in the required form, usually spheres or ribbons, to constitute the regenerator bed.

In the history of magnetocaloric materials, the greatest achievement has been the discovery of the $Gd_5(Ge,Si)_4$ alloy series (Aldrich Prod. Nos. 693510 and 693502). In addition to GMCE, this system shows a very interesting phenomenon known as spontaneous generation of voltage (SGV).[23] SGV occurs in the vicinity of first-order magneto-structural phase transition, which is also responsible for the giant magnetocaloric effect, colossal magnetostriction, and giant magneto-resistance. Materials which show SGV are promising multifunctional miniature sensors capable of sensing changes in temperature, magnetic field, and pressure. Increasing research in this field is expected to yield many similar systems.

Intermetallic alloys without rare earths also can show giant MCE.[24] In addition, there are a few ceramic systems found to be promising for magnetic refrigeration. Work is ongoing to understand the magneto-caloric efficiency of several materials in amorphous, nanocrystalline, single crystalline, thin film and molecular forms, though most do not possess a giant magnetocaloric effect. There is intense activity in the field of molecular magnets in general and molecular magnetic refrigerants in particular and research on magnetocaloric effect now encompasses materials belonging to a wide range of sizes, geometries, and crystalline forms.

Though several potential materials have been developed in recent past, elemental gadolinium (Aldrich Prod. No. 263087) remains the standard reference material for comparing MCE. Advantages of gadolinium are: 1) its moment is quite high, thereby giving rise to a reasonably large entropy change; 2) the S-state nature of the 4f orbital enables it to be free from any large crystal field effects, which would be undesirable for a good refrigerant; and 3) its magnetic ordering temperature is relatively high (close to room temperature) at least among various 4f metals. In many materials, though the magnetic entropy change is quite substantial, their adiabatic temperature change is too low to be considered for these applications. Another drawback of certain materials such as FeRh is that their MCE is irreversible and as such they cannot find a place in a practical refrigerator. Applications of magnetic materials are not just restricted to cooling. Certain materials are known to show an inverse magnetocaloric effect, which implies that the application of the field increases the magnetic entropy and are expected to be useful in devices such as heat pumps. Apart from $Gd_5(Si,Ge)_4$ compounds, other important systems identified so far include: $La(Fe,M)_{13}$ (M=Si, Al); $MnFe(P_{1-x}As_x)$; MnAs; full Heusler alloys, namely Ni_2MnX (X=Sn, In, Sb); and molecular magnets.[25]

The projected applications of magnetic refrigeration are quite wide ranging from air conditioning to food preservation, liquefaction of gases, and cryogenic detectors. Thin film-based magnetic refrigerators are expected to be valuable for miniature devices. Another field where biocompatible magnetocaloric materials can play a role is in medical applications, i.e., as hyperthermia. Growth of the field of MCE has resulted in the exploration of other novel cooling techniques such as the electrocaloric,[26] elastocaloric,[27] and barocaloric[28] effects.

Table 1. Magnetocaloric properties (isothermal entropy change and adiabatic temperature change) of certain potential magnetic refrigerant materials for a field change of 50 kOe.

Material	Magnetic Transition Temperature (K)	Isothermal Magnetic Entropy Change $(\Delta S_m)_{max}$ [J/kg K]	Adiabatic Temperature Change $(DT_{ad})_{max}$ [K]
$Gd_5Si_2Ge_2$	276	20	15
$ErCo_2$	35	36	9.5
$LaFe_{11.57}Si_{1.43}$	188	24	7.5
$MnAs_{0.75}Sb_{0.25}$	235	25	10
NiCoMnSb	250–300	30	—
$La_{0.87}Sr_{0.13}MnO_3$	197	5.8	—
Gd	292	11	11.2

In addition to the role as active (working) materials in a refrigerator, certain magnetic materials serve as passive magnetic regenerators. The difference is that while active materials take part directly in cooling through the field cycle, the latter use their large heat capacities to absorb or desorb heat throughout the thermal cycle. These materials have appreciable magnetic heat capacity associated with magnetic transition at temperatures where phononic and electronic contributions are very small. Research in the field of magnetic refrigerants has also led to identification of several such passive materials that are quite useful in extending the temperature span of a refrigerator, especially to low temperatures. Examples of such materials include the rare-earth intermetallic compounds Gd-Er-Rh, R-Co, and R-Ni.

Future Application Areas for Magnetic Materials

In addition to the exploitation of change in specific heat of a material under the influence of a magnetic field, one can also search for a change in electrical resistivity. This change can be huge in some systems, resulting in transition from a parent insulating magnetic material to a metallic ferromagnet. In this case, change in resistivity is called colossal magnetoresistance (CMR). Several transition metal oxides are known to undergo this kind of field-induced insulator to metal transition, resulting in CMR. There are a large number of metallic and ceramic (both in bulk and thin film form) systems that show large magnetoresistance suitable for applications like field sensing.[29]

A large number of magnetic materials are being prepared in amorphous form for applications related to soft materials. They can be important in the synthesis of nano-structured materials by giving proper heat treatments. Magnetic impedance and magneto-optics are two other fields of great importance today. Magneto-optics deals with change in the polarization of light by a magnetic field, either internal or external. This is of great potential in magnetic recording. Nano/Bio/Molecular magnetism is another field that has recently attracted much attention, as have ferrofluids, colloidal suspensions of ferro/ferri magnetic particles.[30]

In summary, the scope of magnetic materials research is constantly expanding. Discovery of new phenomena, increasing understanding of magnetism, the availability of novel and sophisticated experimental probes, utilization of advanced theoretical and computational tools, and identification of new materials have all contributed to the growth of this field. It is quite certain that many of the present challenges for commercialization will soon be overcome.

References
(1) Goldman, A., *Modern Ferrite Technology*: Springer **2006**.
(2) Buschow, K.H.J., *Rep. Prog. Phys.*, **1977**, *40*, 1179.
(3) Daniel, E.D.; Mee, C.D.; Clark, M.H., *Magnetic Recording: The First 100 Years*: Wiley **1998**.
(4) Mee, C.D.; Daniel, E.D., *Magnetic Recording Technology*: McGraw Hill Professional **1996**.
(5) Stipe, B.C., et. al., *Nature Photonics,* **2010**, *4*, 484.
(6) Tudosa, I., et. al., *Nature*, **2004**, *428*, 831.
(7) Mangin, S., et. al., *Nature Materials*, **2006**, *5*, 210.
(8) Qin, G.W., et. al., *Int. Mat. Rev.*, **2009**, *54*, 157.
(9) Bailbich, M.N., et. al., *Phys. Rev. Lett.*, **1988**, *61*, 2472.
(10) Grünbert, P., et. al., *Phys. Rev. Lett.*, **1986**, *57*, 2442.
(11) Parkin, S.S., et. al., *Nature Materials*, **2004**, *3*, 862.
(12) Shinjo, T., *Magnetism and Spintronics*: Elsevier **2009**.
(13) Hu, J.M.; Li, Z.; Chen, L.-Q.; Nan, C.-W., *Nature Comm.*, **2011**, *2*, 1564/1.
(14) Ohno, H., *Nature Materials*, **2010**, *9*, 952.
(15) Huan, H.C.; Cao, Q.Q.; Zhang, C.L.; Ma, S.C.; Chen, S.Y.; Wang, D.H.; Du, Y.W., *Appl. Phys Lett.*, **2010**, *96(10)*, 202502/1-202502/3.
(16) Engdahl, E.G., *Handbook of Giant Magnetostrictive Materials*: Academic Press **2000**.
(17) Hunter, D.; Osborn, W.; Wang, K.; Kazantseva, N.; Hattrick-Simpers, J.; Takahashi, R.; Yang, H.; Lee, M., *Nature Commun.*, **2013**, *2*, 518.
(18) O'Handley, R.C.; Allen, S.M., in *Encyclopedia of Smart Materials*: Wiley **2002**.
(19) Takeuchi, I.; Famodu, O.O.; Read, J.C.; Aronova, M.A.; Chang, K.-S.; Craciunescu, C.; Lofland, S.E.; Wuttig, M.; Wellstood, F.C.; Knauss, L., *Nature Materials*, **2003**, *2(3)*, 180.
(20) Tishin, A.M.; Spichkin, Y.I., *The Magnetocaloric Effect and its Applications*: IOP Publishers **2003**.
(21) Pecharsky V.K.; Gschneidner Jr., K.A., *Phys. Rev. Lett.*, **1997**, *78*, 4494.
(22) Singh, N.K.; Suresh, K.G.; Nigam, A.K.; Malik, S.K.; Coelho, A.A.; Gama, S., *J. Mag. Mag. Mat.*, **2007**, *317(1-2)*, 68.
(23) Levin, E. M.; Pecharsky, V. K.; Gschneidner, K. A., *Physical Review B*, **2001**, *63(17)*, 174110/1.
(24) Suresh, K.G., *Phys. Express*, **2012**, *2*, 1.
(25) Langley, S.K.; Chilton, N.F.; Moubaraki, B.; Hooper, T.; Brechin, E.K.; Evangelisti, M.; Murray, K.S., *Chem. Sci.*, **2011**, *2(6)*, 1166.
(26) Mischenko, A.S.; Zhang, Q.; Scott, J.F.; Whatmore, R.W.; Mathur, N.D., *Science*, **2006**, *311(5765)*, 1270.
(27) Bonnot, E.; Romero, R.; Manosa, L.; Vives, E.; Planes, A., *Phys. Rev. Lett.*, **2008**, *100(12)*, 125901.
(28) Manosa, L.; Gonzalez-Alonso, D.; Planes, A.; Bonnot, E.; Barrio, M.; Tamarit, J.-L.; Aksoy, S.; Acet, M., *Nature Materials*, **2010**, *9(6)*, 478.
(29) Tokura, Y., *Colossal Magnetoresistive Oxides*: Gordon and Breach **2000**.
(30) Odenbach, S., *Magnetoviscous Effects in Ferrofluids*: Springer **2002**.
(31) Computer Desktop Encyclopedia

For questions, product data, or new product suggestions, contact Aldrich Materials Science at **matsci@sial.com**.

ALDRICH Materials Science

65

Magnetic Oxides

For a complete list of available materials, visit aldrich.com/magnetic.

Name	Purity (%)	Particle Size	Form	Prod. No.
Barium ferrite	98	−325 mesh	powder	383295-250G 383295-1KG
Strontium ferrite	99.5	−325 mesh	powder	480371-25G
Iron(II,III) oxide	99.99	-	powder	518158-10G 518158-50G
Iron(II,III) oxide	95	<5 µm	powder	310069-25G 310069-500G 310069-2.5KG
Iron(III) oxide	-	30 - 50 mesh	powder	371254-50G 371254-250G
Iron(II) oxide	99.9	−10 mesh	powder	400866-5G 400866-25G
Iron(III) oxide	99.999	-	powder	529311-5G 529311-25G
Cobalt(II,III) oxide	99.995	-	calcined (to achieve maximum oxidation)	203114-5G
Cobalt(II,III) oxide	-	<10 µm	powder	221643-50G 221643-250G
Manganese(IV) oxide	99.99	-	solid	203750-5G 203750-25G
Manganese(II) oxide	99	−60 mesh	powder	377201-500G
Manganese(III) oxide	99	−325 mesh	powder	377457-250G 377457-1KG
Manganese(II,III) oxide	97	−325 mesh	powder	377473-100G
Manganese(II) oxide	≥99.99	-	powder and chunks	431761-1G 431761-10G
Manganese(III) oxide	99.99	-	solid	463701-5G 463701-25G
Manganese(IV) oxide	≥99.99	-	powder and chunks	529664-5G 529664-25G

Solution Deposition Precursors for Magnetic Thin Film Formation

For a complete list of available materials, visit aldrich.com/mnel.

Name	Composition	Purity (%)	Form	Prod. No.
Chromium(II) acetate, dimer monohydrate	$[(CH_3CO_2)_2Cr \cdot H_2O]_2$	-	powder	238015-10G
Chromium(III) acetate hydroxide	$(CH_3CO_2)_7Cr_3(OH)_2$	-	powder	318108-250G 318108-1KG
Chromium(III) acetylacetonate	$Cr(C_5H_7O_2)_3$	99.99	-	574082-5G 574082-25G
Chromium(III) acetylacetonate	$Cr(C_5H_7O_2)_3$	97	-	202231-5G 202231-100G
Chromium(III) tris(2,2,6,6-tetramethyl-3,5-heptanedionate)	$Cr(OCC(CH_3)_3CHCOC(CH_3)_3)_3$	-	-	468223-1G
Cobalt(II) acetate	$(CH_3CO_2)_2Co$	99.995	crystals and lumps	399973-1G 399973-10G
Cobalt(II) acetate tetrahydrate	$(CH_3COO)_2Co \cdot 4H_2O$	99.999	powder and chunks	437875-1G 437875-10G
Cobalt(II) acetylacetonate	$Co(C_5H_7O_2)_2$	97	powder and chunks	227129-50G 227129-250G
Cobalt(II) acetylacetonate hydrate	$Co(C_5H_7O_2)_2 \cdot xH_2O$	-	powder or crystals	344613-50G
Cobalt(III) acetylacetonate	$Co(C_5H_7O_2)_3$	99.99	granular powder or crystals	494534-5G 494534-25G
Cobalt(III) acetylacetonate	$Co(C_5H_7O_2)_3$	98	powder or crystals	C83902-25G C83902-100G
Cobalt(II) 2-ethylhexanoate solution	$[CH_3(CH_2)_3CH(C_2H_5)CO_2]_2Co$	-	liquid	444545-100ML 444545-500ML
Cobalt(II) hexafluoroacetylacetonate hydrate	$Co(C_5HF_6O_2)_2 \cdot xH_2O$	98	powder or crystals	339695-5G
Hexamethyldisilane	$(Si(CH_3)_3)_2$	98	liquid	217069-5G 217069-10G 217069-50G
Iron(II) acetate	$Fe(CO_2CH_3)_2$	≥99.99	-	517933-5G 517933-25G
Iron(II) acetate	$Fe(CO_2CH_3)_2$	95	-	339199-10G 339199-50G
Iron(II) acetylacetonate	$[CH_3COCH=C(O)CH_3]_2Fe$	99.95	-	413402-10G
Iron(III) acetylacetonate	$Fe(C_5H_7O_2)_3$	≥99.9	-	517003-10G 517003-50G
Iron(III) acetylacetonate	$Fe(C_5H_7O_2)_3$	≥97.0	-	44920-100G 44920-500G

Name	Composition	Purity (%)	Form	Prod. No.
Iron(III) acetylacetonate	$Fe(C_5H_7O_2)_3$	97	-	F300-25G F300-100G F300-500G
Iron(III) tris(2,2,6,6-tetramethyl-3,5-heptanedionate)	$Fe[(CH_3)_3CCOCHCOC(CH_3)_3]$	-	-	468207-1G
Platinum(II) acetylacetonate	$Pt(C_5H_7O_2)_2$	99.99	-	523038-1G
Platinum(II) acetylacetonate	$Pt(C_5H_7O_2)_2$	97	-	282782-500MG 282782-5G
Tantalum(V) butoxide	$Ta(OCH_2CH_2CH_2CH_3)_5$	99.99	liquid	383333-10G
Tantalum(V) ethoxide	$Ta(OC_2H_5)_5$	99.98	-	339113-10G 339113-100G
Tantalum(V) methoxide	$Ta(OCH_3)_5$	-	solid	383244-5G
Tetraethyl orthosilicate	$Si(OC_2H_5)_4$	99.999	-	333859-25ML 333859-100ML
Tetraethyl orthosilicate	$Si(OC_2H_5)_4$	98	-	131903-25ML 131903-250ML 131903-500ML 131903-1L 131903-2.5L 131903-4L
Tetramethyl orthosilicate	$Si(OCH_3)_4$	≥99	-	341436-25G 341436-100G
Tetramethyl orthosilicate	$Si(OCH_3)_4$	98	-	218472-100G 218472-500G
Tetrapropyl orthosilicate	$(CH_3CH_2CH_2O)_4Si$	95	-	235741-25G 235741-100G
Tris(ethylenediamine)cobalt(III) nitrate	$(H_2NCH_2CH_2NH_2)_3Co(NO_3)_3$	≥99.99	-	529532-25G
Zirconium acetate solution	-	-	liquid	413801-500ML 413801-2L
Zirconium(IV) acetate hydroxide	$(CH_3CO_2)_xZr(OH)_y$, x+y ~4	-	powder	464600-100G 464600-500G
Zirconium(IV) acetylacetonate	$Zr(C_5H_7O_2)_4$	98	powder	338001-25G 338001-100G
Zirconium(IV) bis(diethyl citrato)dipropoxide	-	-	liquid	515817-1L
Zirconium(IV) butoxide solution	$Zr(OC_4H_9)_4$	-	solution	333948-100ML 333948-500ML 333948-2L
Zirconium(IV) *tert*-butoxide	$Zr[OC(CH_3)_3]_4$	99.999	-	560030-5G 560030-25G
Zirconium(IV) ethoxide	$Zr(OC_2H_5)_4$	97	-	339121-5G 339121-25G
Zirconium(IV) isopropoxide isopropanol complex	$Zr(OCH(CH_3)_2)_4 \cdot (CH_3)_2CHOH$	99.9	powder	339237-10G 339237-50G
Zirconium(IV) propoxide solution	$Zr(OCH_2CH_2CH_3)_4$	-	solution	333972-5ML 333972-100ML 333972-500ML
Zirconium(IV) propoxide solution	$Zr(OCH_2CH_2CH_3)_4$	-	-	96595-100ML 96595-500ML
Zirconium(IV) silicate	$ZrSiO_4$	-	powder	383287-250G 383287-1KG
Zirconium(IV) trifluoroacetylacetonate	$Zr(C_5H_4F_3O_2)_4$	97	-	383325-1G

For questions, product data, or new product suggestions, contact Aldrich Materials Science at **matsci@sial.com**.

ALDRICH®
Materials Science

67

ALDRICH®
Materials Science

Aldrich® Materials Science Congratulates

Dr. John A. Rogers

Recipient of the MRS Mid-Career Researcher Award

The Materials Research Society (MRS) has selected John A. Rogers, director of the Seitz Materials Research Laboratory at the University of Illinois at Urbana-Champaign (UIUC), to receive the 2013 Mid-Career Researcher Award "for fundamental and applied contributions to materials, mechanics designs, and assembly techniques for stretchable/flexible electronic systems."

The MRS Mid-Career Researcher Award, endowed by Aldrich Materials Science, recognizes exceptional achievements in materials research made by mid-career professionals.

About Dr. Rogers

Dr. John A. Rogers obtained his BA and BS degrees in chemistry and in physics from the University of Texas at Austin. From MIT, he received SM degrees in physics and in chemistry and a Ph.D. in physical chemistry. He has published nearly 400 papers and holds over 80 patents. Rogers is a Fellow of MRS, IEEE, APS, and AAAS, and a member of the National Academy of Engineering. His research has been recognized with many awards, including a MacArthur Fellowship in 2009 and the Lemelson-MIT Prize in 2011.

aldrich.com/midcareeraward

SIGMA-ALDRICH®